The Spitzer Matching Survey of the UltraVISTA Ultra-deep Stripes (SMUVS)

Deshmukh, S.; Caputi, K. I.; Ashby, M. L. N.; Cowley, W. I.; McCracken, H. J.; Fynbo, J. P. U.; Le Fèvre, O.; Milvang-Jensen, B.; Ilbert, O.

[Link to publication in University of Groningen/UMCG research database](#)

The *Spitzer* Matching Survey of the UltraVISTA Ultra-deep Stripes (SMUVS): The Evolution of Dusty and Nondusty Galaxies with Stellar Mass at $z = 2$–6

S. Deshmukh[1] , K. I. Caputi[1] , M. L. N. Ashby[2] , W. I. Cowley[1], H. J. McCracken[3] , J. P. U. Fynbo[4] , O. Le Fèvre[5], B. Milvang-Jensen[6] , and O. Ilbert[5]

[1] Kapteyn Astronomical Institute, University of Groningen, P.O. Box 800, 9700AV Groningen, The Netherlands; deshmukh@astro.rug.nl
[2] Harvard-Smithsonian Center for Astrophysics, 60 Garden Street, Cambridge, MA 02138, USA
[3] Institut d'Astrophysique de Paris, CNS & UPMC, UMR 7095, 98 bis Boulevard Arago, F-75014, Paris, France
[4] Cosmic Dawn Center (DAWN), Niels Bohr Institute, University of Copenhagen, Juliane Maries vej 30, DK-2100 Copenhagen, Denmark
[5] Aix Marseille Université, CNRS, LAM (Laboratoire d'Astrophysique de Marseille), UMR 7326, F-13388, Marseille, France
[6] Dark Cosmology Centre, Niels Bohr Institute, University of Copenhagen, Juliane Maries Vej 30, DK-2100 Copenhagen, Denmark
Received 2017 December 9; revised 2018 August 7; accepted 2018 August 10; published 2018 September 13

Abstract

The *Spitzer* Matching Survey of the UltraVISTA Ultra-deep Stripes (SMUVS) has obtained the largest ultradeep *Spitzer* maps to date in a single field of the sky. We considered the sample of about 66,000 SMUVS sources at $z = 2$–6 to investigate the evolution of dusty and nondusty galaxies with stellar mass through the analysis of the galaxy stellar mass function (GSMF), extending previous analyses about one decade in stellar mass and up to $z = 6$. We further divide our nondusty galaxy sample with rest-frame optical colors to isolate red quiescent ("passive") galaxies. At each redshift, we identify a characteristic stellar mass in the GSMF above which dusty galaxies dominate, or are at least as important as nondusty galaxies. Below that stellar mass, nondusty galaxies compose about 80% of all sources, at all redshifts except at $z = 4$–5. The percentage of dusty galaxies at $z = 4$–5 is unusually high: 30%–40% for $M_* = 10^9$–$10^{10.5} M_\odot$ and $>80\%$ at $M_* > 10^{11} M_\odot$, which indicates that dust obscuration is of major importance in this cosmic period. The overall percentage of massive ($\log_{10}(M_*/M_\odot) > 10.6$) galaxies that are quiescent increases with decreasing redshift, reaching $>30\%$ at $z \sim 2$. Instead, the quiescent percentage among intermediate-mass galaxies (with $\log_{10}(M_*/M_\odot) = 9.7$–10.6) stays roughly constant at a $\sim 10\%$ level. Our results indicate that massive and intermediate-mass galaxies clearly have different evolutionary paths in the young universe and are consistent with the scenario of galaxy downsizing.

Key words: galaxies: evolution – galaxies: high-redshift – galaxies: luminosity function, mass function – infrared: galaxies

1. Introduction

Dust has increasingly been recognized as a key element in galaxy growth, being the by-product of stellar evolution and a catalyst for the formation of molecular hydrogen (e.g., Gould & Salpeter 1963; Hollenbach & Salpeter 1971; Gavilan et al. 2012). Because of this, analyzing the presence of dust in galaxies at different redshifts can shed light on fundamental aspects of galaxy evolution (e.g., Calura et al. 2017; Popping et al. 2017). Although the dust content in present-day galaxies is known to be moderate, the role of dust was much more important in the past, as was tentatively inferred already two decades ago (e.g., Hughes et al. 1998; Adelberger & Steidel 2000) and more recently shown by multiple observational studies conducted with mid- and far-IR telescopes (e.g., Caputi et al. 2007; Gruppioni et al. 2010; Magnelli et al. 2011).

Despite significant progress, the nature of dust and the presence of dusty galaxies at high redshifts are not well understood. While theoretical models are successful in producing massive dusty/passive galaxies, they find it challenging to reproduce their number counts, their physical properties, and their $z = 0$ stellar mass functions *simultaneously* (e.g., Gabor et al. 2011; Casey et al. 2014; Feldmann et al. 2017; see also Section 4.1.3 in Somerville & Davé 2015).

The task of determining the dust content of galaxies at moderate to high redshifts has proven to be quite challenging. Given the limited sensitivity of mid-/far-IR telescopes, identifying the presence of dust in a wide range of galaxies at different redshifts requires a different approach. An alternative option to direct observations is to model the galaxy spectral energy distribution (SED), as dust extinction is usually considered as a free parameter for the fitting. This method has been followed by multiple authors from low to high redshifts (e.g., Pannella et al. 2009; Cucciati et al. 2012). In parallel, through either SED fitting or color selections, different works have attempted to identify quiescent galaxies, i.e., galaxies whose levels of star formation activity can be considered negligible with respect to the amount of stars formed at previous times (e.g., Kajisawa et al. 2011; Cassata et al. 2013; Sommariva et al. 2014; Straatman et al. 2014; Martis et al. 2016).

The *Spitzer* Matching Survey of the UltraVISTA Ultra-deep Stripes (SMUVS; M. Ashby et al. 2018, in preparation) is a *Spitzer* (Werner et al. 2004) Exploration Science Program, which has obtained ultradeep 3.6 and 4.5 μm imaging with the Infrared Array Camera (IRAC; Fazio et al. 2004) in the COSMOS field (Scoville et al. 2007). SMUVS has been designed to complement the UltraVISTA ultradeep near-IR survey (McCracken et al. 2012) in the region with deepest optical coverage. Currently, SMUVS is the largest quasi-contiguous *Spitzer* field suitable to study the high-z universe. Its unique combination of area and depth allows us to investigate different aspects of galaxy evolution with an unprecedented level of statistics and dynamic range at high redshifts.

In this paper we analyze the large SMUVS galaxy sample, containing a total of $\sim 66,000$ galaxies at $z = 2$–6. We conduct
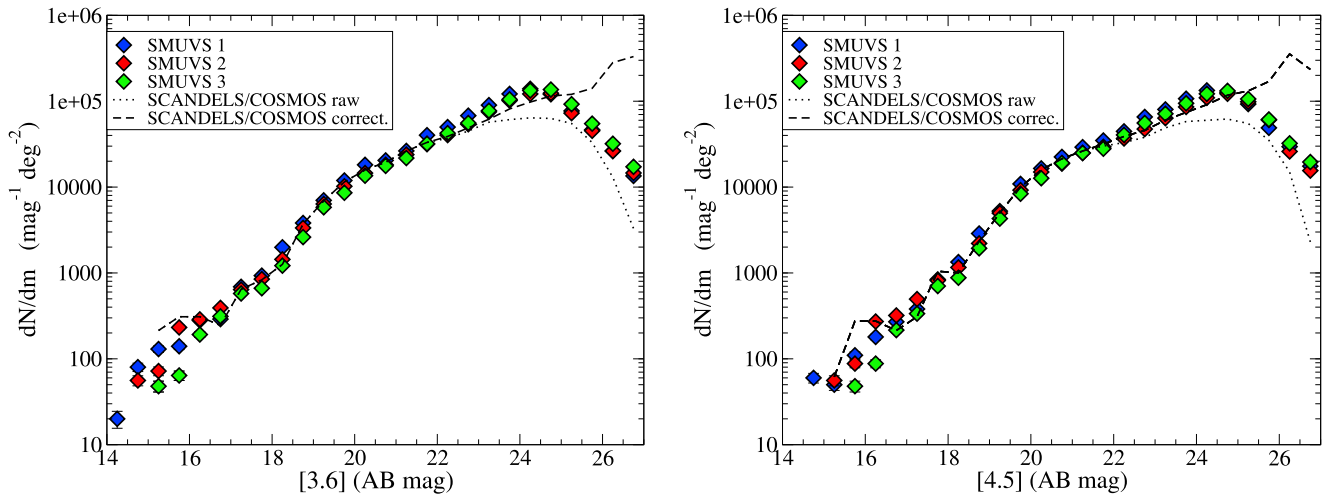
Figure 1. SMUVS number counts obtained using the UltraVISTA HK_s source positions as priors. Left: IRAC channel 1 (3.6 μm). Right: IRAC channel 2 (4.5 μm). The corrected SCANDELS/COSMOS number counts are based on the Helgason et al. (2012) models.

an unprecedented analysis of the evolution of galaxies with and without significant dust extinction (dusty and nondusty galaxies hereafter) as a function of stellar mass spanning the period between $\sim$1 and 3.2 Gyr after the big bang. In parallel, in other companion papers we analyze the clustering properties of the SMUVS galaxies over a similar redshift range (Cowley et al. 2018) and study star formation in galaxies at $z = 4$–5 as inferred from their Hα excess in the IRAC 3.6 μm band (Caputi et al. 2017). In addition, an independent work included the SMUVS data to trace the progenitors of present-day massive galaxies out to $z = 5$ (Hill et al. 2017).

This paper is organized as follows. In Section 2 we describe the utilized data sets and source catalog construction, and in Section 3 we explain our derivation of galaxy properties, including photometric redshifts and stellar masses. We present the galaxy stellar mass function (GSMF) of dusty and nondusty galaxies in Section 4, and we analyze the overall number densities of dusty/nondusty sources, as well as the evolution to quiescence, among massive and intermediate-mass galaxies in Section 5. Finally, in Section 6 we present our concluding remarks. Throughout this paper we adopt a cosmology with $H_0 = 70$ km s^{-1} Mpc^{-1}, $\Omega_M = 0.3$, and $\Omega_\Lambda = 0.7$. All magnitudes and fluxes are total, with magnitudes referring to the AB system (Oke & Gunn 1983). Stellar masses correspond to a Chabrier (2003) initial mass function (IMF).

2. Data Sets and Source Catalog

As part of the SMUVS program (PI Caputi; M. Ashby et al. 2018, in preparation), we have collected ultradeep *Spitzer* 3.6 and 4.5 μm data in the COSMOS field (Scoville et al. 2007), over an area overlapping the three UltraVISTA ultradeep stripes (McCracken et al. 2012) with the deepest optical coverage from the Subaru telescope (Taniguchi et al. 2007). The SMUVS mosaics considered in this paper correspond to the almost final depth of the survey, which reaches on average an integration time of $\sim$25 hr per pointing (including IRAC ancillary data in COSMOS; Sanders et al. 2007; Ashby et al. 2013, 2015; Steinhardt et al. 2014). These long integration times, coupled to the large IRAC point-spread function (PSF) FWHM, which is about 1$\farcs$9, imply that the resulting SMUVS images suffer from severe source confusion. Therefore, we apply a technique that

includes source deblending in order to measure the IRAC photometry. We proceed as follows.

First, we construct UltraVISTA HK_s average stack maps of the three relevant ultradeep stripes, which we use as priors in the IRAC PSF fitting. The UltraVISTA data considered here correspond to the third data release (DR3), which in the ultradeep stripes reaches an average depth of $K_s = 24.9 \pm 0.1$ and $H = 25.1 \pm 0.1$ (2$''$ diameter; 5σ).[7] We extract the HK_s sources using the software SExtractor (Bertin & Arnouts 1996) with a detection threshold of 1.5σ over 5 contiguous pixels. Using these source positions, we measure their photometry on the SMUVS 3.6 and 4.5 μm mosaics, applying a PSF-fitting technique with the DAOPHOT package on IRAF. This PSF-fitting technique (applied in the task "allstar") consists of fitting the photometry of groups of sources simultaneously and iteratively until the fluxes are deblended and the residuals are minimized. In order to maximize the number of detected sources through PSF fitting, we run "allstar" twice: a first run is done on each original image, and a second pass is done on each residual image.

For the PSF-fitting technique, we make use of empirical images of the PSF, which we construct from stars in the field, in each stripe separately. With the PSF-fitting algorithm, we achieve convergence for $\sim$70% of the sources, after the two passes described above. This degree of convergence is normal, given that we are trying to PSF-fit sources down to very faint levels (based on the known UltraVISTA coordinates). For the remaining $\sim$30% of sources, we directly measure IRAC aperture fluxes in 2$\farcs$4 diameter circular apertures at the UltraVISTA positions. We correct these aperture fluxes to total fluxes by multiplying them by a factor of 2.13, which is determined from the curves of growth of stars in the field. In total, we find that 95%–96% of all UltraVISTA ultradeep sources are detected in at least one IRAC band, and 93%–94% in both bands. In the following, we refer to the UltraVISTA ultradeep sources with at least one IRAC detection as the "SMUVS sources."

As we explain in detail in Section 3, we do not use the IRAC photometry for the SED fitting of sources with potentially significant light contamination in any of the IRAC bands. This

---

[7] See http://www.eso.org/sci/observing/phase3/data_releases/uvista_dr3.pdf.

applies to <14% of our sources. This criterion allows us to minimize the impact that any IRAC light contamination can have on the derived source properties.

Figure 1 shows the SMUVS 3.6 and 4.5 μm number counts obtained using the UltraVISTA sources as priors. The results for the three stripes are in very good agreement among themselves and indicate that our resulting SMUVS catalogs are 80% (50%) complete at [3.6] and [4.5] = 25.5 (26.0) total magnitudes. Note that this completeness is higher than that obtained with the raw counts in the SCANDELS/COSMOS field (Ashby et al. 2015), in spite of the latter images being deeper on average. This is because the SCANDELS/COSMOS number counts have been obtained from a direct source extraction using no priors, and because detections at both 3.6 and 4.5 μm have been imposed to consider a source reliable. Our prior UltraVISTA detection makes the criterion of two IRAC detections unnecessary to guarantee the source reliability.

We have independently checked the number counts completeness limits by performing simulations similarly to those in Caputi et al. (2011). However, in contrast to this work, in which there was only a direct source extraction on the IRAC images, here we need to emulate our IRAC photometric extraction based on the UltraVISTA source priors. For this, in our simulations we proceeded as follows: we created a catalog of 50,000 mock sources using the IRAF task "galllist," following a power-law distribution between magnitudes 17 and 28. We then created a set of 10 mock UltraVISTA HK_s images (using IRAF MKOBJECTS), based on the original HK_s mosaics, in each of which we inserted 5000 of the mock sources without repetition. We then ran SExtractor with the same parameter values used for the original HK_s mosaics and compiled the recovered mock sources. These recovered mock sources were used as priors to be inserted in the IRAC images. We created a set of mock IRAC mosaics, based on the original mosaics, in which we inserted no more than 500 of the recovered mock sources at a time (we did not add more sources per image to avoid altering the confusion properties). We then used the IRAF DAOPHOT package at the position of the known prior sources, as in our original methodology. To have HK_s magnitudes corresponding with the IRAC magnitudes, we have considered the color distribution of the real SMUVS sources in different magnitude bins. The final number count completeness levels as a function of mag are the product of the completeness obtained in the SExtracted recoverery of mock sources in the HK_s-band mosaic and the completeness on the IRAC photometry measurements using priors (where, at each IRAC magnitude, we applied weights to take into account the real source [HK_s–IRAC] color distributions). From this combined calculation, we get that at IRAC mag = 25.5 (26.0) we have 76% (59%) completeness, which is very similar to the completeness levels derived from comparison with the Helgason et al. (2012) models (Figure 2).

For all the SMUVS sources, we measure 2″ diameter circular photometry on 26 broad, intermediate, and narrow bands, namely, CFHT U band; Subaru B, V, r, i^+, z^+, z^{++}, $IA427$, $IA464$, $IA484$, $IA505$, $IA527$, $IA574$, $IA624$, $IA679$, $IA709$, $IA738$, $IA767$, $IA827$, $NB711$, and $NB816$; HST $F814W$; and UltraVISTA Y, J, H, and K_s. We use SExtractor in dual-image mode with the UltraVISTA HK_s stacks as detection images. We correct the measured aperture fluxes to total fluxes by applying point-source aperture corrections in each band. In addition, we correct all our photometry for Galactic extinction.
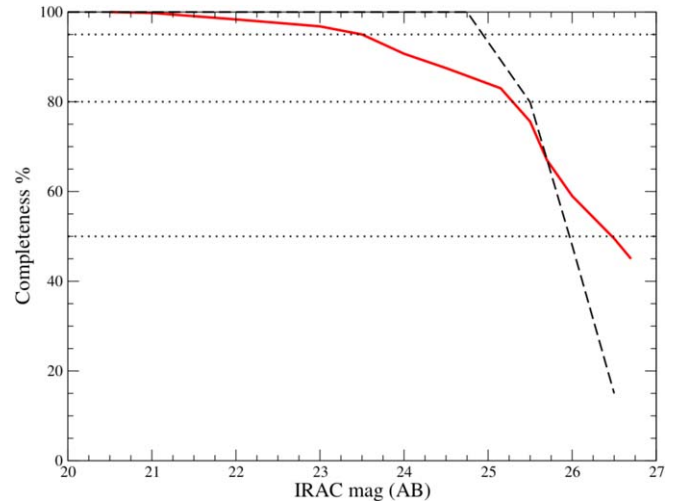

Figure 2. SMUVS source completeness as derived from mock galaxy simulations (red solid line; see text for details). The completeness derived from the IRAC number count comparison with the Helgason et al. (2012) models is also shown (black dashed line). The horizontal dotted lines indicate the 95%, 80%, and 50% completeness limits for reference.

To determine errors on the photometry, we perform empty-aperture statistics in different parts of each stripe.

Following Caputi et al. (2011), we clean our catalog for galactic stars, using SExtractor's stellarity parameter and a (J − [3.6]) versus (B − J) color–color diagnostic (Figure 3). We discard all sources with an HK_s-based stellarity parameter greater than 0.8 that lie on the stellar sequence clearly defined on the (J − [3.6]) versus (B − J) diagram. These rejected stars constitute ∼2% of the original SMUVS sources detected using the UltraVISTA priors. We also mask regions of contaminated light around the brightest sources to obtain a clean catalog of UltraVISTA ultradeep sources with at least one IRAC-band detection, over a net area of 0.66 deg^2. This is the catalog with 28-band photometry (U through K_s + IRAC) that we consider as input for the SED-fitting analysis.

The PSF-fitting technique assumes that all sources are point-like. This is a reasonable assumption for virtually all IRAC sources with [3.6] > 21 mag (see Figure 25 in Ashby et al. 2013). Besides, this approach is consistent with all our other multiwavelength photometry, measured on circular apertures (and corrected to total), which also implicitly assumes that all sources are point-like. Some other methods to derive IRAC photometry (e.g., Merlin et al. 2015) do take into account the shape of resolved sources, and this may be preferable for the study of low-z galaxies, as many of them are resolved even in the IRAC bands. Here, however, we only focus on the analysis of $z > 2$ sources, and thus the point-like source assumption can safely be adopted.

3. SMUVS Galaxy Properties Determined from SED Fitting

3.1. Photometric Redshifts

To perform the source SED fitting, we run the χ^2-minimization code LEPHARE (Arnouts et al. 1999; Ilbert et al. 2006) on our catalog with total fluxes, based on 2″ aperture photometry for all bands U through K_s, and obtained as described above for the IRAC bands. As in Caputi et al. (2015), in the case of nondetections we adopt 3σ flux upper limits in the broad bands, also determined from empty-aperture statistics (up to the K_s band), and ignored narrow and intermediate bands, as well as any IRAC
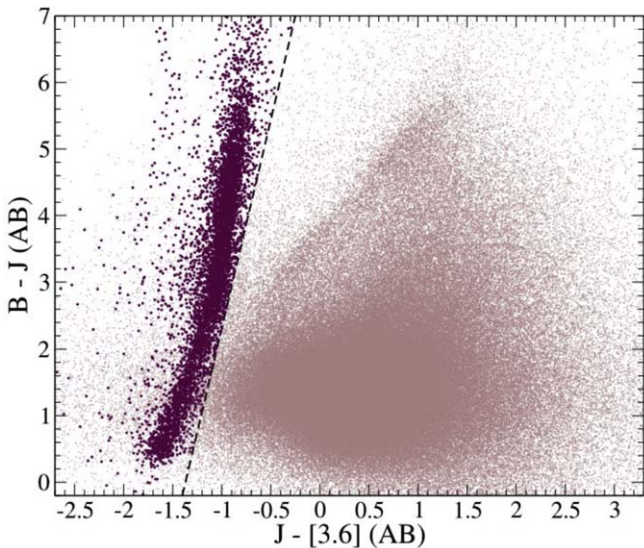
Figure 3. $J - [3.6]$) vs. $(B - J)$ color–color diagram for the SMUVS sources extracted with UltraVISTA HK_s priors. Galactic stars appear clearly segregated on the left-hand side of this plot.

band with a nondetection. Note that this nondetection treatment is only done for true SExtractor nondetections. Each time that SExtractor extracts a meaningful (positive) flux, we leave that flux measurement, even if it has a large associated error bar. Within LEPHARE, we choose the following option: all SED templates that produce fluxes higher than the 3σ upper limits in the bands with nondetections are automatically discarded.

To minimize the chances of affecting the SED fitting due to contamination in the IRAC photometry, we impose the following: for the sources with an IRAC (3.6 or 4.5 μm) magnitude >22 having an IRAC neighbor with a magnitude <23 within less than 3 arscec radius, we do not utilize the IRAC photometry in the SED fitting (we only used the 26 bands from U through K_s). This situation applies to $<14\%$ of all SMUVS sources, and only 12% at $2 < z < 6$. Comparison of the photometric redshifts obtained with and without IRAC photometry for these sources, with respect to spectroscopic redshifts in COSMOS, indicates that excluding the IRAC photometry is the right approach in this case.

We use a series of synthetic templates from the Bruzual & Charlot (2003) library, namely, a simple stellar population and different exponentially declining star formation histories with star formation timescales $\tau = 0.01, 0.1, 0.3, 1.0, 3.0, 5.0, 10.0,$ and 15 Gyr. Each synthetic spectrum is attenuated with the Calzetti et al. (2000) reddening law, leaving the color excess as a free parameter with possible values $E(B - V) = 0.0$–1.0 in steps of 0.1. Adopting a finer color excess grid does not have any significant impact on our results.[8] The Calzetti et al. reddening law appears to be the most suitable for high-z galaxies (Cullen et al. 2018). We run LEPHARE with emission lines and iterate to obtain photometric zero-point corrections, which significantly improves the overall quality of our photometric redshifts, as determined from the comparison with spectroscopic redshifts, when available (see discussion below). All zero-point corrections are $\lesssim 0.1$ mag in absolute value, except in the V band, for which we derive a correction of -0.18 mag.

---

[8] For the low stellar mass dusty galaxies, the differences in the GSMF between our adopted extinction grid and a more refined one are larger than the error bars, but still very small ($\lesssim 0.1$–0.2 dex).
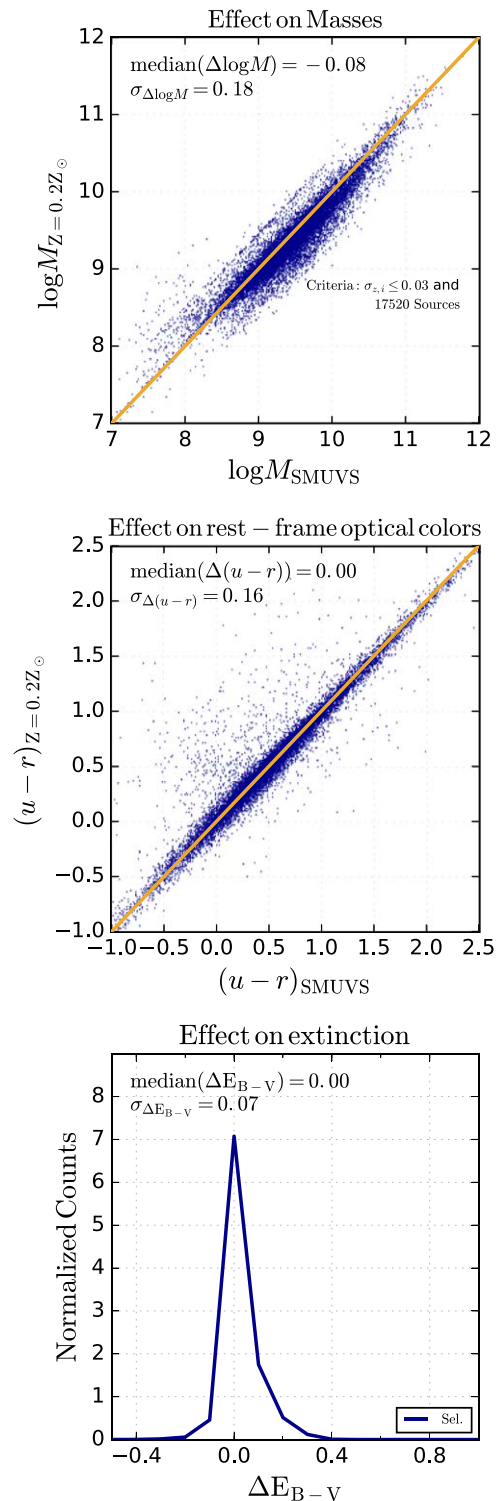
Figure 4. Impact of allowing subsolar metallicities on masses, rest-frame optical colors, and extinction. The comparison has been made for sources with $|z_{Z_\odot} - z_{0.2Z_\odot}|/(1 + z_{Z_\odot}) \leqslant 0.03$, ensuring that we do not carry differences produced by very different redshifts.

Our strategy for photometric redshift determination is as follows. We first run LEPHARE using only spectral templates with solar metallicity. For galaxies with a primary redshift solution $z_{phot} < 5$, we consider that the best solar-metallicity template was the final best-fit model. Instead, for galaxies with a best-fit redshift $z \geqslant 5$, we reran LEPHARE using an equivalent

Figure 5. Redshift distribution of our SMUVS galaxy sample. The inset zooms in the redshift range considered for scientific analysis in this paper.
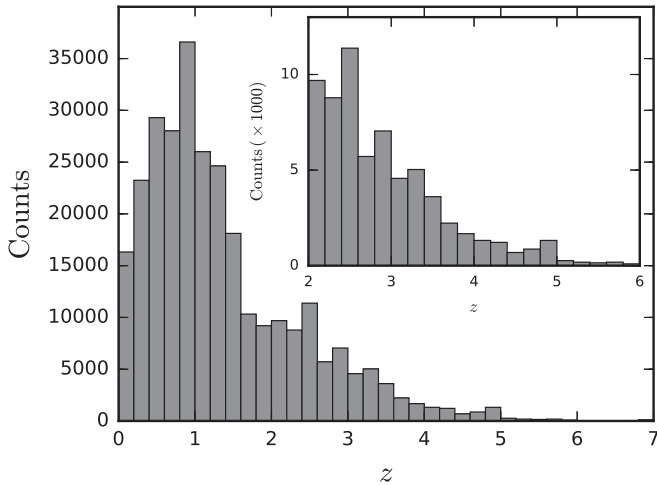

Figure 6. Comparison between our z_{phot} and existing z_{spec} for $\sim$13,000 SMUVS galaxies. The color scale indicates the log-density of sources.

set of templates with a subsolar metallicity, namely, $Z = 0.2\,Z_\odot$. We compare the minimum reduced χ^2 obtained with both metallicity runs and adopt as a best fit the model that provides the absolute smallest χ^2 value. In total, about 34% of the $z_{phot} \geqslant 5$ prefer a model with subsolar metallicity. The redshift cut to consider only $Z = Z_\odot$, or both $Z = Z_\odot$ and $Z = 0.2\,Z_\odot$, has been calibrated through the comparison of the resulting best photometric redshifts with spectroscopic redshifts, as described in the next paragraph. The approach of considering the possibility of subsolar metallicities only at $z \geqslant 5$ does not introduce any significant bias in our results. Figure 4 shows the compared rest $(u - r)$, $E(B - V)$, and stellar mass values obtained when considering two possible metallicity values (0.2 $Z_\odot$ and $Z_\odot$) also at $z < 5$, versus our values obtained with fixed metallicity. These plots show that the biases in these properties are negligible or very small compared with the corresponding error bars, and the scatter is also small.

From LEPHARE's runs we obtain photometric redshifts and stellar mass estimates for >99% of our sources. For the remaining <1%, LEPHARE indicated that a stellar template yielded a lower minimum reduced χ^2 than any galaxy template in the SED fitting. We discard these sources from our sample. We also exclude a small percentage of sources <1% because their best z_{phot} were incompatible with their detection at short wavelengths, i.e., they have a >2σ U-band detection and a redshift $z_{phot} > 3.6$, a >2σ B_J-band detection and $z_{phot} > 4.6$, or a >2σ V_J-band detection and $z_{phot} > 5.6$ (see Caputi et al. 2015). Our final SMUVS output catalog with photometric redshift determinations contains 288,003 galaxies. In Figure 5 we show the resulting redshift distribution. The inset zooms in the redshift range considered for scientific analysis in this paper, i.e., $z = 2$–6, which contains about 66,000 SMUVS galaxies.

We use the large amount of spectroscopic data available in COSMOS (e.g., Lilly et al. 2007; Comparat et al. 2015; Le Fèvre et al. 2015) to assess the quality of our obtained photometric redshifts. Figure 6 shows the resulting z_{phot} versus z_{spec} diagnostic, which is based on more than 13,000 galaxies (including 627 at $z_{spec} > 2$). These make for $\sim$4% of our SMUVS sources ($\sim$1% at $z > 2$). We have not replaced the photometric redshifts of those galaxies with spectroscopic redshifts. Given the very small percentage of $z > 2$ sources
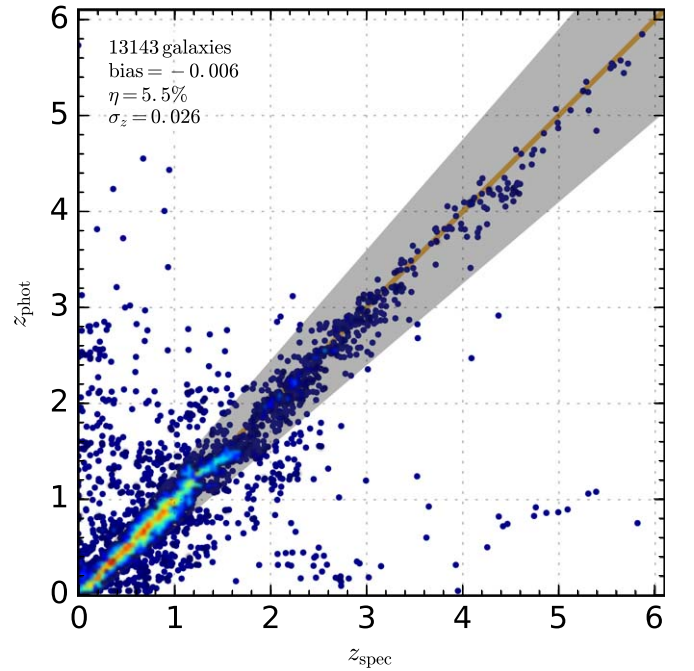
with spectroscopic information, the impact of not introducing this change is negligible in all our analyses. We find a negligible bias ($\equiv$median($z_{phot}-z_{spec}$)) in our photometric redshifts. All galaxies lying outside the gray shaded area are considered outliers, which are defined as those sources for which $\sigma_i = |z_{phot,i} - z_{spec,i}|/(1 + z_{spec,i}) > 0.15$. We find that only $\sim$5% of sources are outliers according to this criterion and that the remaining ones show a tight z_{phot}–z_{spec} correlation, i.e., $\sigma_z = \mathrm{std}(\sigma_i) = 0.026$. The negligible bias, small σ_z, and small outlier fraction (η) show that our photometric redshifts are of excellent quality. These values are broadly consistent with those obtained by other authors in the literature, although in most cases the number of galaxies with spectroscopic redshifts utilized in the literature diagnostic is less than half than the number used here (except in Laigle et al. 2016, where the total number of considered sources with spectroscopic redshifts is comparable to ours). Considering only the sources with $z_{spec} > 2$, the bias and σ_z are still small (-0.089 and 0.032, respectively), but the fraction of outliers rises to $\sim$16%.

3.2. Stellar Masses

Figure 7 shows the best-fit stellar masses M_* versus z_{phot} obtained from LEPHARE for the SMUVS galaxies. This figure shows that our galaxy sample spans more than four decades in stellar mass, from 10^7 through >$10^{11}\,M_\odot$. To estimate the stellar mass 50% completeness limits at different redshifts, we follow the method described in Tomczak et al. (2014). First, we consider the IRAC limiting magnitude for which our sample can be considered 100% complete, which is $m_{[4.5],lim} \leqslant 24.75$ (see black dashed line in Figure 2), as discussed in Section 2. Then we divided our sample into redshift bins of width $\Delta z = 0.5$, and, in each of them, we work out the limiting stellar mass ($M_{*,lim}$) at which 50% of galaxies with $M_* > M_{*,lim}$ have $m_{[4.5]} < m_{[4.5],lim}$. Similarly, we also estimate the stellar mass 80% and 95% completeness limits at different redshifts. We summarize our results in Table 1.
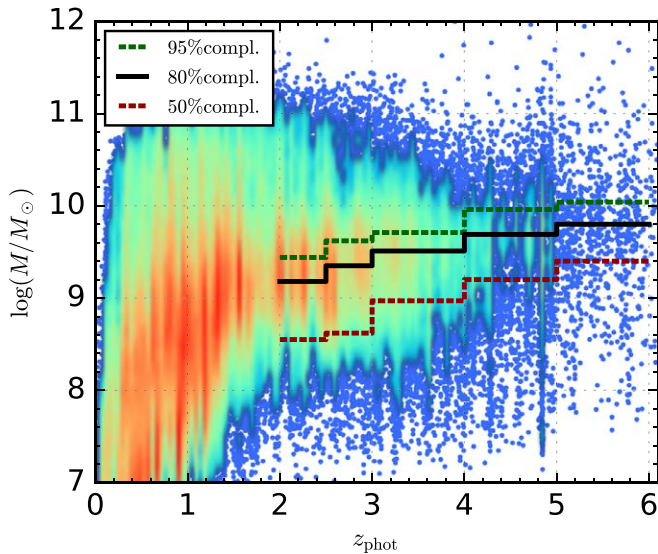
Figure 7. Stellar masses vs. photometric redshifts for all SMUVS galaxies. The green dashed, solid black, and red dashed lines show the 95%, 80%, and 50% completeness limits, respectively. For clarity, high-density (low-density) regions in the plot have been colored red (blue).

Table 1
Stellar Mass 50%, 80%, and 95% Completeness Limits at Different Redshifts

Redshift	50% M_* Limit $\log_{10}(M/M_\odot)$	80% M_* Limit $\log_{10}(M/M_\odot)$	95% M_* Limit $\log_{10}(M/M_\odot)$
2.0–2.5	8.55	9.18	9.44
2.5–3.0	8.62	9.35	9.62
3.0–4.0	8.97	9.51	9.71
4.0–5.0	9.20	9.69	9.96
5.0–6.0	9.40	9.80	10.04

3.3. Selection of Dusty and Nondusty Galaxies

The main goal of this paper is to analyze the stellar mass and redshift evolution of dusty and nondusty galaxies at $z = 2$–6. Our classification is based on the color excess $E(B-V)$ that we obtain from the best-fit SED fitting: we divide our galaxy sample into two groups, one with $E(B-V) \leqslant 0.1$ and another one with $E(B-V) \geqslant 0.2$. These values correspond to V-band extinctions $A_V \lesssim 0.4$ mag and $A_V \gtrsim 0.8$ mag, respectively, for a Calzetti et al. (2000) reddening law. We chose these color excess values to divide the sample such that we have roughly similar numbers of galaxies in the two extinction groups. Across $z = 2$–6 the overall median percentage of nondusty galaxies varies between 40% and 70%, depending on the redshift. Note that, according to our criterion, nondusty galaxies are indeed virtually dust-free, while the dusty group comprises galaxies with moderate to high dust extinctions. This classification in dusty and nondusty galaxies is slightly different from that considered by Martis et al. (2016), who adopted an empirical division in the UVJ color–color diagram that approximately coincides with a dust extinction $A_V = 1$.

Our classification of dusty and nondusty galaxies is robust against degeneracies in parameter space. Figure 8 shows the total probability density distribution versus color excess $E(B-V)$ for a representative sample of 800 dusty and nondusty galaxies in our sample at $z = 2$–6. These probability density distributions are obtained by marginalizing over all other variables. This figure shows that, even considering degeneracies in parameter space, the
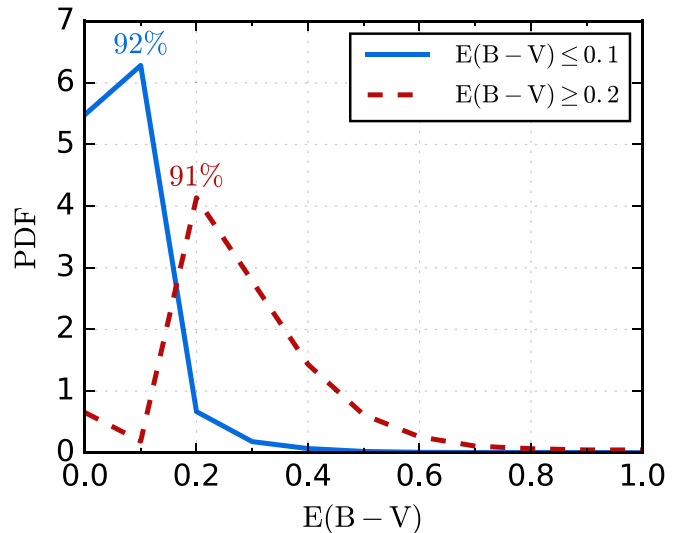

Figure 8. Total probability density distribution vs. color excess $E(B-V)$ for a representative sample of our dusty and nondusty galaxies at $z = 2$–6. These probability density distributions have been obtained by marginalizing over all other variables. The integrated probability density function indicates that dusty (nondusty) galaxies have an overall probability of 0.91 (0.92) of being classified in the correct extinction group.

dusty and nondusty galaxies have an overall probability >0.9 of being in their correct classification group.

4. The GSMF of Dusty and Nondusty Galaxies at $z = 2$–6

The GSMF at high z has recently been studied in the COSMOS field (Ilbert et al. 2013; Muzzin et al. 2013; Caputi et al. 2015; Davidzon et al. 2017) and other fields (e.g., Caputi et al. 2011; Santini et al. 2012; Duncan et al. 2014; Grazian et al. 2015; Song et al. 2016). Here we focus on analyzing the contributions of dusty and nondusty galaxies to the GSMF at $z = 2$–6. In the following we present our results for the two considered galaxy families. As a sanity check, we verify that our total GSMF is consistent with previous works at different redshifts: we show the results of this general comparison in Appendix B.

4.1. Methodology

We compute the GSMF using the $1/V_{\max}$ technique (Schmidt 1968) at different redshifts. Although this technique involves binning the galaxy sample in stellar mass, it has the advantage of being free of any parameter dependence or model assumptions. To compute $V_{\max}$, we need to calculate the maximum redshift $z_{\max}$ at which a source could have been observed given a limiting flux. This is accomplished by solving the following equation for $z_{\max}$:

$$\frac{D_{\text{lum}}^2(z_{\max})}{1 + z_{\max}} = \frac{f_{\nu,\text{obs}}}{f_{\nu,\text{lim}}} \frac{D_{\text{lum}}^2(z_{\text{obs}})}{1 + z_{\text{obs}}}, \qquad (1)$$

where $D_{\text{lum}}(z)$ is the luminosity distance at redshift z and $f_{\nu,\text{obs}}$, $f_{\nu,\text{lim}}$ are the observed and limiting fluxes, respectively. We choose a limiting flux corresponding to a magnitude $[4.5] = 26$ mag (or $[3.6] = 26$ mag, in the case of nondetection at 4.5 μm). For sources fainter than this limiting magnitude, we apply no $V_{\max}$ corrections. In addition to the $V_{\max}$ correction for each galaxy, we apply an incompleteness correction factor $(100\%/x\%)$ considering the $[4.5]$ magnitude of each galaxy (or its $[3.6]$ magnitude in the

case of nondetection at 4.5 μm) and the completeness levels (x%) determined from the Helgason et al. (2012) model (black dashed line) in Figure 2.

We identify three sources of uncertainties in the GSMF calculation, namely, a Poisson error σ_{poi}, an error associated with the SED fitting σ_{mc}, and cosmic variance σ_{cov}. The first one is simply related to the statistics of our galaxy sample. We estimate σ_{poi} using the tabulated values provided in Gehrels (1986). The SED-fitting error is related to the uncertainties in the photometric redshifts and stellar mass determinations. To estimate σ_{mc}, we create 100 mock catalogs. These mock catalogs are obtained by randomizing the photometry of each galaxy (within the photometric uncertainties assuming a Gaussian distribution) and redetermining the masses and redshifts with LEPHARE. We then recompute the GSMF for each of the mock catalogs, and σ_{mc} represents the 16th and 84th percentiles of these mock GSMFs. Finally, to estimate the errors due to cosmic variance, we followed the prescription of Moster et al. (2011). We comment on the contribution of each source of uncertainty in Appendix C.

Note that throughout this paper we only show the GSMF data points down to our estimated 50% stellar mass completeness limits (Table 1). And, as explained above, in the GSMF calculation we have considered all the SMUVS galaxies that result in stellar masses down to these limits (independently of their IRAC magnitudes). This allows us to show the widest possible dynamic range in stellar mass enabled by our data. We have performed a few sanity checks and confirmed the following: (1) if we only consider those galaxies with IRAC < 23.5, which is brighter than the 95% completeness limit, we recover the high-mass end of our GSMF (this is shown as a downward-pointing arrow in our GSMF plots; (2) if we exclude all sources with IRAC mag > 26 (i.e., those sources below the 50% completeness limit of the IRAC catalog), we basically obtain the same GSMF as that shown here. Only in the lowest stellar mass bins do we observe some marginal difference, which is irrelevant, as no conclusion in this paper depends on them. The GSMF data points that include sources with mag >26 are indicated as lower limits in our GSMF plots.

4.2. General Results

Figure 9 shows our GSMF computed with the $1/V_{max}$ method and corrected for completeness for the dusty and nondusty galaxies separately, at different redshifts from $z = 2$ to $z = 6$. On top of each panel, we show the fraction f of the two different populations as a function of stellar mass. We calculate the uncertainties in f considering a binomial distribution. The 50%, 80%, and 95% stellar mass completeness limits at different redshifts are indicated with black upward-pointing arrows in the GSMF panels. All GSMF values for dusty, nondusty, nondusty blue, and nondusty red galaxies are tabulated in Appendix D.

From Figure 9 we can see that, at $z = 2.0$–2.5, dusty and nondusty galaxies contribute similarly to the overall population of galaxies with stellar masses $\gtrsim 10^{10.1}\,M_\odot$. At lower stellar masses, instead, the GSMF is clearly dominated by the nondusty galaxies.

At $z > 2.5$ dusty galaxies start to dominate the GSMF high-mass end, or become comparable in number density to nondusty galaxies, making for 60%–80% of all massive galaxies at these redshifts. The dusty galaxy dominance becomes most evident at $4 < z < 5$. The stellar mass below which nondusty galaxies overtake the dominance evolves with redshift: it is $\approx 10^{10.5}\,M_\odot$ at $z = 3.0$–4.0 (compared to $\approx 10^{10.1}\,M_\odot$ at $z = 2.5$–3.0).

In addition, our results indicate that the period elapsed at $z = 4$–5 was of major importance for dust extinction in galaxy

evolution. Dusty galaxies more clearly dominate the GSMF high-mass end at $M_* \gtrsim 10^{10.6}\,M_\odot$, and their fraction increases steadily with stellar mass, reaching >80% at $M_* > 10^{11}\,M_\odot$. Below $M_* \sim 10^{10.6}\,M_\odot$, nondusty galaxies are more numerous than dusty ones, following the same trend observed at lower redshifts. However, at $z = 4$–5 the percentage of dusty sources among intermediate-mass galaxies is higher than at any later time, i.e., 30%–40% of all intermediate- and low-mass galaxies down to $M \approx 10^9\,M_\odot$. This indicates that significant dust extinction was important not only among massive galaxies but also among many lower-mass galaxies at these redshifts.

In the total GSMF at $z = 2.0$–2.5 (Figure 9 and Appendix B), there is a flat regime at intermediate stellar masses. This feature has previously been identified in the literature at lower redshifts (e.g., Pozzetti et al. 2010; Bielby et al. 2012), implying that the GSMF is best fit by a double Schechter (1976) function rather than a single one. Interestingly, this kind of double functional form is more clearly seen for the nondusty galaxies alone, with our results indicating that this is a feature present since at least $z = 3$.

4.3. Bisection of the Nondusty Galaxy Population

Nondusty objects can be very diverse in nature: some are unobscured star-forming galaxies, while others have no dust because they have virtually ceased their star formation, i.e., they are old and passive (or almost passive) galaxies. These two groups can broadly be divided using rest-frame optical colors, as is commonly done in the literature (although in general these color criteria are applied without separating dusty and nondusty galaxies in the first place).

Figure 10 shows the rest-frame M_r absolute magnitude versus $u - r$ color diagram for our nondusty galaxies at $z = 2.0$–6.0. We compute the absolute magnitudes by applying a k-correction to the filters closest to the rest-frame u and r bands. This method is preferred to the one where the absolute magnitudes are computed directly from SED templates (for a detailed discussion, see Section 4.3 in Davidzon et al. 2017, and references therein). We then classify our nondusty galaxies according to their colors: $u - r < 1.3$ and $u - r \geqslant 1.3$ as the blue and red populations, respectively, following Baldry et al. (2004).

We find that only $\sim$6% of our nondusty galaxies are quiescent, i.e., have a red $u - r$ color. As these galaxies are nondusty, their red optical colors can only be explained by the presence of a prominent 4000 Å break, i.e., they are old galaxies, dominated by stars with ages $\gtrsim$1 Gyr. Perhaps not surprisingly, this minor fraction of red, nondusty sources is very biased in stellar mass: they are mostly massive galaxies, as can be seen in Figure 11. We will discuss massive galaxies further in Section 5.1.

To check for possible contaminants among our classified quiescent galaxies, we have cross-correlated this population with the *Spitzer* COSMOS 24 μm catalog (Sanders et al. 2007) and the C-COSMOS X-ray catalog (Civano et al. 2016). We found that only 1.5% of our classified passive sources are X-ray active galactic nuclei, and only 3% are 24 μm detected, indicating that the fraction of contaminants within our sample is very small.

Almost all of our dusty and nondusty red galaxies (97%–99%) are brighter than IRAC = 26. On the other hand, nondusty blue sources constitute $\sim$96% of the IRAC-faint population (IRAC > 26).

The bisection of the nondusty GSMF into red and blue sources clearly shows the origin of the double Schechter behavior up to $z = 3$: while the low-mass regime is dominated only by blue (very likely star-forming) galaxies, the high-mass regime is made of both
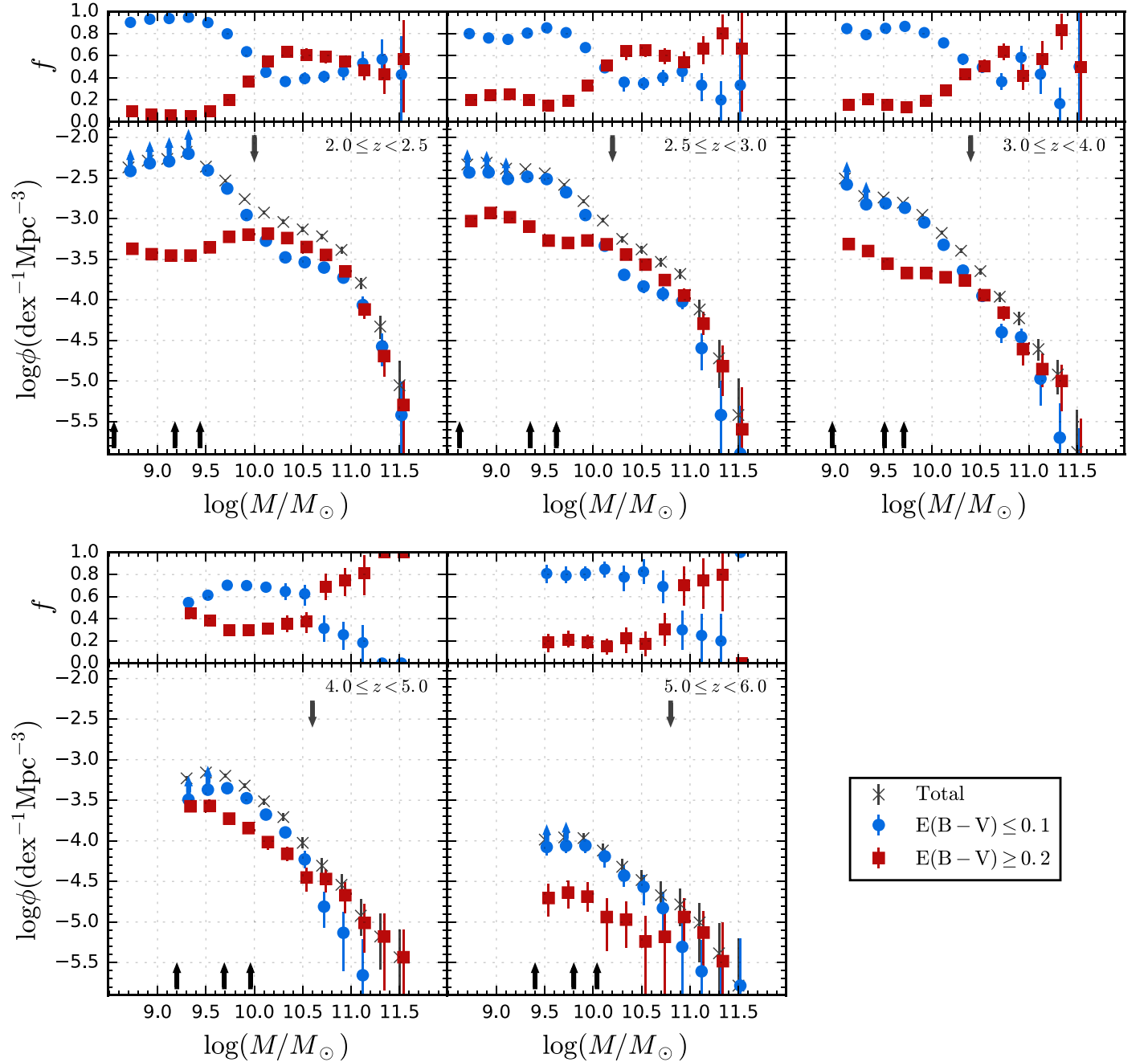
Figure 9. GSMF data points computed with the $1/V_{max}$ technique decomposed into two extinction bins. Error bars include Poisson shot noise, SED-fitting uncertainties, and cosmic variance. The total GSMF is shown with black crosses, and the nondusty and dusty GSMFs are shown with blue filled circles and red filled squares, respectively. The upper panels show the fraction f of nondusty and dusty galaxies with respect to the total GSMF. Black upward-pointing arrows indicate the 50%, 80%, and 95% stellar mass completeness limits. Upward-pointing arrows on the data points indicate bins affected by sources fainter than IRAC = 26. Downward-pointing arrows show the limit at which we recover the high-mass end when considering IRAC < 23.5 sources. Errors on f are determined by considering the variance of a binomial distribution (after incorporating non-Poissonian uncertainties).

blue star-forming galaxies and red old galaxies. This is consistent with what has been found in the literature at lower redshifts (e.g., Pozzetti et al. 2010; Ilbert et al. 2013). More recently, Tomczak et al. (2014) have found a similar result up to $z = 2$, but they did not find an "upturn" in the GSMF at higher redshifts, in spite of analyzing sufficiently deep data to investigate the relevant stellar mass regime. Here, instead, we clearly see this upturn up to $z = 3$ and confirm that this feature is present independently of any V_{max} and incompleteness corrections in our GSMF.

To facilitate the comparison with the galaxy population classification based solely on the rest *UVJ* color–color diagram

adopted by other authors (e.g., Muzzin et al. 2013; Tomczak et al. 2014), we show the locus that each of our classified galaxy populations (dusty; nondusty/blue; and nondusty/red) occupies on that plane (Figure 12). For clarity, we only show our galaxies with $\log_{10} M_*/M_\odot \geqslant 9.7$, which are those that are our main focus of discussion hereafter.

We find that only about one-third of our classified quiescent galaxies lie within the quiescent wedge defined in the literature on the *UVJ* plane. Within our own classification, we recognize many more quiescent galaxies that are close to the wedge but lie outside of it. At the same time, we find that the quiescent
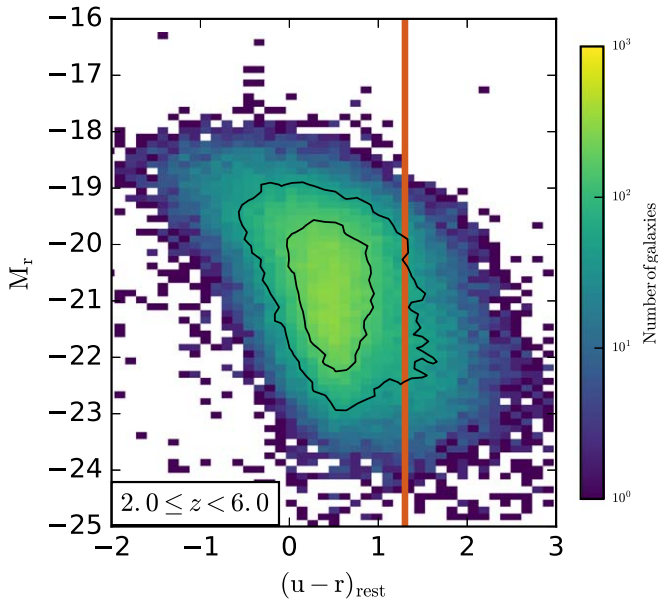
Figure 10. Rest-frame color–magnitude diagram of our sources at $2.0 < z < 6.0$. The contours contain 50% and 80% of our galaxies. The vertical red line corresponds to our color cut (Baldry et al. 2004). The rest-frame colors are derived using the filters closest to rest-frame u and r.

color wedge has significant contamination from dusty sources. Even if these sources can be relatively old (as much as the age of the universe at each given redshift), the presence of significant dust extinction at high z excludes the possibility that these galaxies can be strictly passive: a significant amount of dust extinction in the SED fitting implies that there is a significant amount of intrinsic UV photons, which can only be explained through significant star formation or nuclear activity. In summary, if we applied a simple UVJ color–color selection to classify quiescent galaxies, we would select a population that, according to our SED-fitting results based on 28-band information, has ~40% nonquiescent galaxies and at the same time misses two-thirds of them (according to our quiescent definition based on SED fitting adopted here). So we can conclude that the two methodologies would select two different subsamples of "quiescent galaxies." Through the UVJ diagram one can mainly select galaxies with low specific star formation rates (e.g., Fumagalli et al. 2014), while our own methodology selects a population of galaxies for which the red rest-frame $(u - r)$ colors are only explained by age rather than dust, i.e., galaxies that are more settled into a "red and dead" phase.

Of course, one could argue that for many sources lying around the borders of the UVJ passive wedge, the typical errors in the photometry (which are $\gtrsim 0.15$ for all ground-based colors) could explain the different classification. In fact, this the main reason why one should consider the alternative approach proposed here to select quiescent galaxies: by taking into account the entire photometric information, the full SED-fitting classification can compensate for the errors that may affect a particular color.

5. The Overall Fractions of Dusty/Nondusty Galaxies and the Evolution to Quiescence

5.1. Massive Galaxies

In this section we focus on the analysis of the population of massive galaxies with $\log_{10} M_*/M_\odot \geqslant 10.6$. Figure 13 shows

the cumulative number density of galaxies with stellar masses above this threshold versus redshift. As before, we separate our sample into dusty and nondusty galaxies, and the latter group was further divided according to their optical colors. Our derived number densities are also listed in Table 2.

We see that, at $z = 4$–5, the population of massive galaxies is dominated by galaxies with high dust extinction. At $z \sim 2$ the total number density of massive galaxies is more than a factor of 10 larger than at $z = 4$–5, and the dusty and nondusty populations become similar in number density. By analyzing the number density evolution, we infer that a possible explanation for this behavior is that the dusty massive galaxies at $z \sim 4$–5 evolve into nondusty sources by $z \sim 3.5$ (both number densities are very similar), while at the same time new dusty ones are being created. Similarly, the dusty galaxies at $z \sim 3.5$ could become nondusty by $z \sim 3$, while further dusty ones are created, and this process continues at least down to $z = 2$.

Among the nondusty galaxies, the blue and red populations evolve at different rates with cosmic time. While the number density of blue nondusty galaxies grows by 1 dex between $z \sim 5.5$ and $z \sim 2$, the number density of red nondusty galaxies increases by 2 dex in this same period. Our red nondusty galaxies are, by definition, a very good proxy for quiescent galaxies.[9] Therefore, this means that the population of massive quiescent galaxies has grown by a factor of ~100 in the ~2 Gyr elapsed between $z = 5.5$ and $z = 2$.

The number density evolution of blue and red nondusty galaxies shown in Figure 13 suggests that it is unlikely that dusty galaxies could have evolved into red nondusty (quiescent) galaxies directly. If there is an evolutionary link between these massive galaxy populations, then the most likely sequence is dusty (star-forming) → blue nondusty (star-forming) → red nondusty (quiescent). This would be consistent with a scenario in which massive galaxies passed by a nondusty star-forming phase before becoming quiescent objects. A plausible physical mechanism for stripping massive galaxies of their dust and subsequently quenching star formation are high-velocity outflows driven by black hole accretion (e.g., Hopkins et al. 2016). Our galaxy number densities suggest that this transition from dusty into blue nondusty takes about 0.5–1.0 Gyr. In any case, although this proposed evolutionary scenario is compatible with our derived galaxy number densities, our results can certainly not exclude other possible paths for massive galaxy evolution.

In Figure 13 we also compare the number density of our red nondusty massive galaxies with the number density of passive galaxies selected in the literature for the same (or a very similar) stellar mass cut (Mancini et al. 2009; Muzzin et al. 2013; Straatman et al. 2014; Tomczak et al. 2014; Davidzon et al. 2017; Merlin et al. 2018). These passive galaxy selections are based on rest-frame colors, and their number densities are directly quoted by the authors, or we have obtained them by integrating their corresponding GSMF.[10] Our comparison shows that the number density of our red nondusty

---

[9] Strictly, determining the passive nature requires spectroscopy to confirm the absence of significant emission lines. However, our selection criterion of being red and nondusty naturally selects galaxies dominated by old stellar populations. In this sense, our classification is better than selections based only on color cuts to identify quiescent galaxies, which, as we have shown, have significant contamination from dusty sources.

[10] In the latter case we integrate the Schechter fits to the GSMF. The uncertainties on the number densities reflect the uncertainties on the Schechter parameters. This method was implemented by Muzzin et al. (2013), Tomczak et al. (2014), and Davidzon et al. (2017).
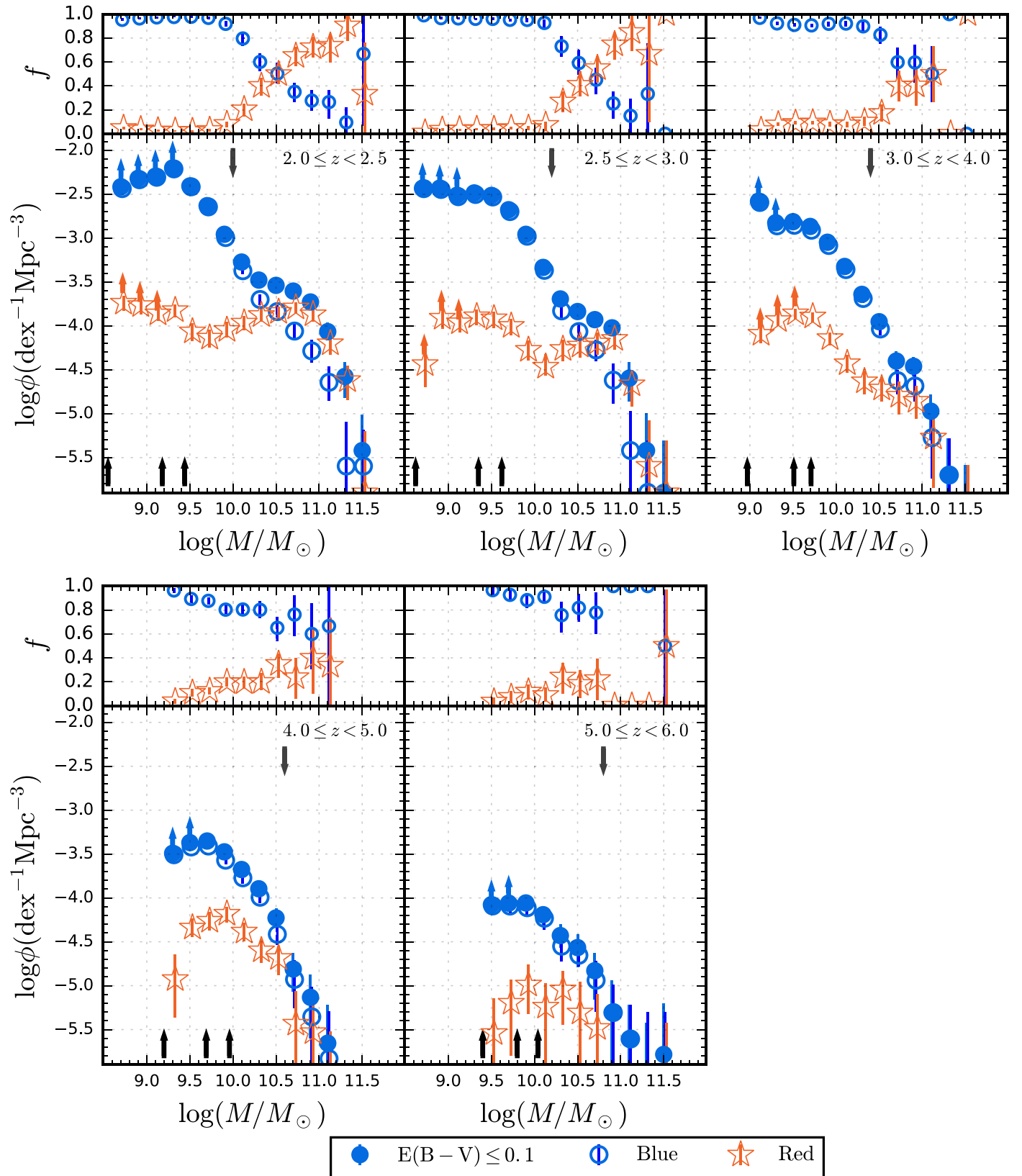
Figure 11. Decomposition of the nondusty GSMF for blue and red galaxies. We show the total nondusty GSMF (blue filled circles) for reference, as well as the GSMF of the blue and red populations (blue open circles and red stars, respectively). The upper panels show the fraction of blue and red galaxies in the nondusty sample. Black upward-pointing arrows indicate the 50%, 80%, and 95% stellar mass completeness limits. Upward-pointing arrows on the data points indicate bins affected by sources fainter than IRAC = 26. Downward-pointing arrows show the limit at which we recover the high-mass end when considering IRAC <23.5 sources.

Dusty

Non-dusty / blue
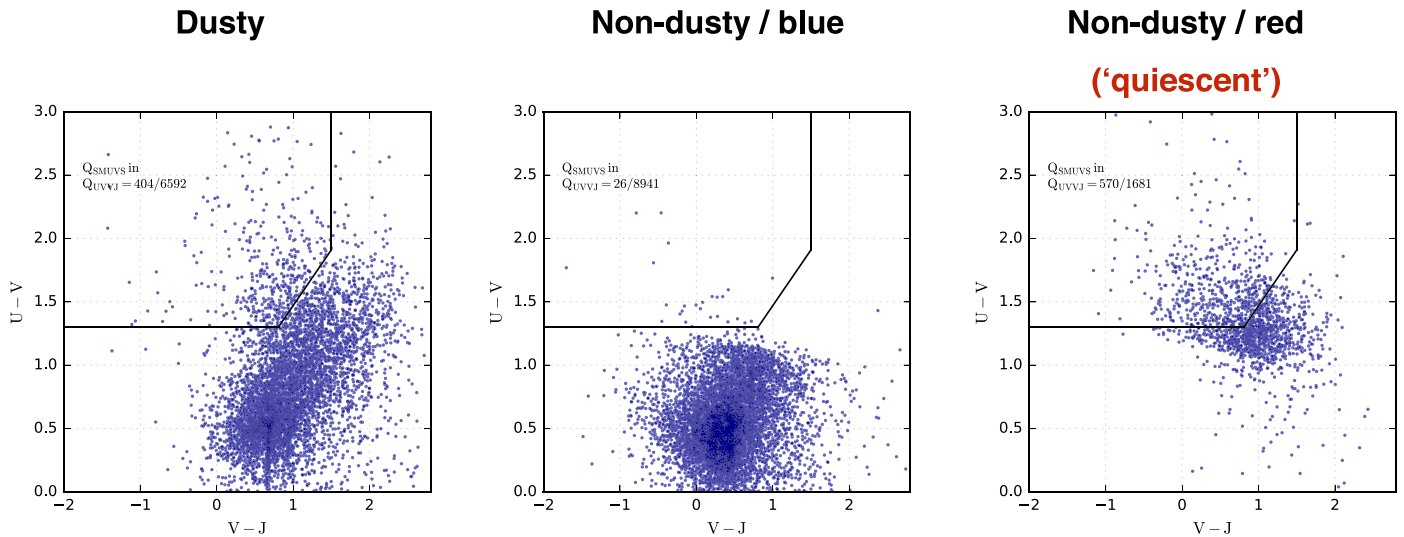
Non-dusty / red

('quiescent')

Figure 12. Location of our three classified galaxy populations (dusty, nondusty/blue, and nondusty/red) in the rest *UVJ* color–color diagram, showing the wedge utilized by other authors to segregate "quiescent galaxies." For clarity, we only show our galaxies with $\log_{10} M_*/M_\odot \geqslant 9.7$, which are those that are the main focus of discussion in this paper. These plots show that only about one-third of our classified quiescent galaxies lie within the *UVJ* quiescent wedge. We recognize many more quiescent galaxies that are close to the wedge but lie outside of it (right panel). At the same time, we find that the quiescent color wedge has significant contamination from dusty sources (left panel). Our nondusty/blue sources virtually all lie outside of the wedge, as expected (middle panel).
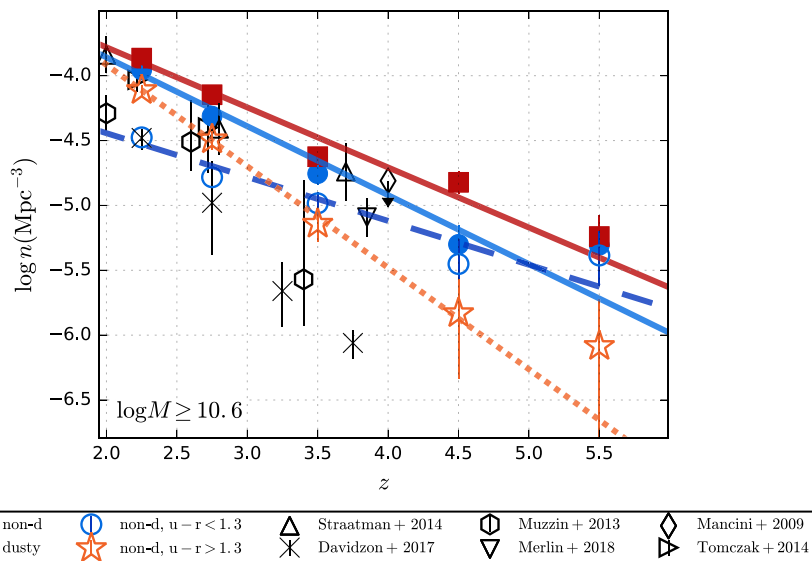

Figure 13. Number densities *n* of massive galaxies (i.e., those with $\log_{10} M_{st} > 10.6 \, M_\odot$) vs. redshift. We show *n* separately for different galaxy populations: dusty (squares), all nondusty (filled circles), red nondusty (stars), and blue nondusty (open circles). We show linear fits for each population. For a comparison, we plot the number densities of quiescent galaxies derived by Mancini et al. (2009), Muzzin et al. (2013), Straatman et al. (2014), Tomczak et al. (2014), Davidzon et al. (2017), and Merlin et al. (2018).

galaxies is significantly higher than the number density of passive galaxies derived from Muzzin et al. (2013) and Davidzon et al. (2017) GSMFs. These differences are mainly produced by the shallower depths of the data sets used by these authors with respect to our own. In the case of the comparison with Davidzon et al. (2017), there is the effect of (a) their choice of dust extinction law and (b) their specific criterion to select passive galaxies, which is color based, but different from that applied by other authors. Davidzon et al. (2017) also correct for Eddington bias (Eddington 1913), which causes a drop in number densities at the massive end of the GSMF.

Our red nondusty galaxy number densities are broadly consistent with the value derived by Merlin et al. (2018) and the upper limit from Mancini et al. (2009). They are also in excellent agreement with the number densities derived by

Straatman et al. (2015) at $z \sim 2$–3, although this might be somewhat fortuitous, given their very different methodology to select quiescent galaxies. At higher redshifts, instead, our results indicate a much faster decline in the number density of passive galaxies than that obtained by these authors. This difference does not seem to be the product of the different methodologies (note that we would select *less* rather than more passive galaxies using the quiescent wedge of the *UVJ* diagram, according to Figure 12). The observed differences could in part be the result of cosmic variance, as Straatman et al. (2014) analyzed images over an area $\sim$6.5 times smaller than that considered here.

Figure 14 shows the fractions of our different populations (dusty, nondusty/blue, and nondusty/red, i.e., quiescent) among all massive ($\log_{10} M_*/M_\odot > 10.6$) galaxies, versus redshift. We compare these fractions to those obtained in the literature. In these

Table 2
Number Densities of Massive ($\log_{10} M_*/M_\odot > 10.6$) Galaxies

Redshift	n_{dusty} (all) $10^{-4} \times$ Mpc^{-3}	$n_{nondusty}$ (all) $10^{-4} \times$ Mpc^{-3}	$n_{nondusty}$ (blue) $10^{-4} \times$ Mpc^{-3}	$n_{nondusty}$ (red) $10^{-4} \times$ Mpc^{-3}
2.25	$1.366^{+0.107}_{-0.107}$	$1.107^{+0.101}_{-0.082}$	$0.335^{+0.053}_{-0.050}$	$0.773^{+0.080}_{-0.068}$
2.75	$0.713^{+0.077}_{-0.078}$	$0.487^{+0.058}_{-0.071}$	$0.165^{+0.041}_{-0.032}$	$0.322^{+0.051}_{-0.054}$
3.50	$0.238^{+0.033}_{-0.033}$	$0.176^{+0.029}_{-0.027}$	$0.104^{+0.023}_{-0.021}$	$0.072^{+0.020}_{-0.019}$
4.50	$0.151^{+0.031}_{-0.029}$	$0.050^{+0.022}_{-0.017}$	$0.035^{+0.020}_{-0.015}$	$0.015^{+0.012}_{-0.010}$
5.50	$0.058^{+0.027}_{-0.028}$	$0.049^{+0.025}_{-0.018}$	$0.041^{+0.022}_{-0.017}$	$0.008^{+0.012}_{-0.008}$

other works, quiescent galaxies have been selected using the *UVJ* color–color diagram wedge. In addition, Martis et al. (2016) have also determined regions to segregate dusty and nondusty star-forming galaxies on this color–color plane.

We find that our fractions of massive galaxies classified in the different groups at $2 < z < 3$ are in good agreement, within the error bars, with the fractions reported by Martis et al. (2016). Our fraction of quiescent galaxies at these redshifts also broadly agrees with the fraction obtained from Tomczak et al. (2014) and Straatman et al. (2015), although the error bars in the fractions derived from these other works are very large.

5.2. Intermediate-mass Galaxies

Figure 15 is analogous to Figure 13, but for intermediate-mass galaxies. Here we only analyze the stellar mass range $9.7 \leqslant \log_{10} M_*/M_\odot \leqslant 10.6$ to ensure high stellar mass completeness across all the analyzed redshifts ($\gtrsim 80\%$ up to $z = 5$, and $\sim 70\%$ completeness at $z = 5$–6). In any case, all our quoted number densities carry completeness corrections, even if they are very small. These derived number densities are listed in Table 3.

We clearly see that the number density evolution of dusty and nondusty intermediate-mass galaxies is very different from that of massive galaxies. At all redshifts $z > 2.5$, blue nondusty galaxies dominate the population with intermediate stellar masses. Only at $z = 2$ does the population of dusty sources become equally important (in number) to the blue nondusty galaxies. This is in contrast to the fractions observed among massive galaxies, in which the balance between dusty/nondusty sources is fairer at $z = 2$–4 and dominated by dusty galaxies at $z > 4$. These results are consistent with the conclusions of Martis et al. (2016), who found that intermediate stellar mass galaxies are predominantly unobscured star-forming objects at $z \sim 3$, while the high-mass galaxy population is dominated by dusty star-forming sources.

Another striking difference for intermediate-mass galaxies is that the percentage of red nondusty (i.e., quiescent) sources is low and almost constant at all redshifts. Indeed, we obtain that quiescent sources constitute only $\sim 10\%$ of these galaxies at $z = 2$–6, which suggests that star formation quenching and evolution into quiescence is a much slower process among intermediate-mass galaxies than among massive ones. Our findings are consistent with the results of Sommariva et al. (2014), who reported a decline in the fraction of quiescent galaxies at faint near-IR magnitudes, corresponding to stellar masses $\lesssim 10^{10.8} M_\odot$.

6. Summary and Conclusions

We have studied the evolution of dusty and nondusty galaxies with stellar mass at $z = 2$–6, considering the $\sim 66{,}000$ SMUVS sources present in this redshift range. We classified

our galaxies into dusty/nondusty according to their color excess $E(B - V)$, as obtained with the best SED-fitting solution. Furthermore, we divided the nondusty sample using rest-frame optical colors to isolate the sample of quiescent galaxies (here defined as those galaxies whose red colors can only be explained by the dominance of old stellar populations).

For an overall statistical analysis, we computed the GSMF of our galaxy samples in different redshift bins between $z = 2$ and $z = 6$. We found that, at $z = 2.0$–2.5, dusty and nondusty galaxies contribute similarly to the overall population of galaxies with stellar masses $\gtrsim 10^{10.1} M_\odot$. At $z > 2.5$, instead, dusty galaxies dominate the GSMF high-mass end, making for 60%–80% of all massive galaxies. The stellar mass below which nondusty galaxies dominate evolves with redshift: it is $\approx 10^{10.5}$ ($10^{10.1}$) $M_\odot$ at $z = 3.0$–4.0 ($z = 2.5$–3.0). The increasing importance of dust extinction with stellar mass is in agreement with the results of previous studies (Reddy et al. 2012; Heinis et al. 2013).

At lower stellar masses the GSMF is clearly dominated by the nondusty galaxies. At all the analyzed redshifts, except at $z = 4$–5, nondusty galaxies make for $\sim 80\%$ of intermediate-mass galaxies. At $z = 4$–5, instead, this percentage is somewhat lower, i.e., $\sim 60\%$–70%. At this cosmic epoch, dusty galaxies appear to be at the maximum of their importance: they constitute 30%–40% of the galaxies with $M_* = 10^9$–$10^{10.5} M_\odot$ and $>80\%$ of those with $M_* > 10^{11} M_\odot$.

We also analyzed the evolution of quiescent galaxies among massive and intermediate-mass galaxies (with $\log_{10}(M_*/M_\odot) \geqslant 10.6$ and $\log_{10}(M_*/M_\odot) = 9.7$–10.6, respectively) versus cosmic time. We found that the fraction of passive galaxies had a fast increase between $z \sim 6$ and $z \sim 2$, rising from $<10\%$ to $\sim 30\%$, which indicates that the mechanisms that quenched the star formation activity among massive galaxies were very effective in the first few billion years of cosmic time. In remarkable contrast, the quiescent galaxy percentage among intermediate-mass galaxies stays rather constant at a $\sim 10\%$ level in this redshift range. These results are in line with the idea of *galaxy downsizing* (e.g., Brinchmann & Ellis 2000; Kodama et al. 2004; Juneau et al. 2005; Cattaneo et al. 2008) and show that massive and intermediate-mass galaxies clearly had different evolutionary paths over the first few billion years of cosmic time.
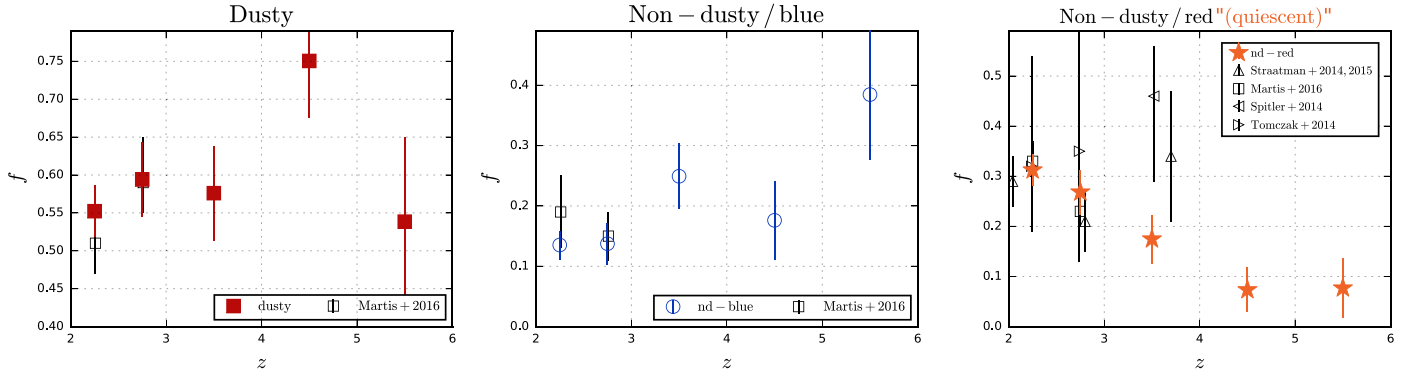
Figure 14. Comparison of our fractions of massive ($\log_{10} M_*/M_\odot > 10.6$) galaxies with different classifications, with the fractions of similar populations from the literature. In contrast with our methodology, all literature works cited here have selected quiescent galaxies using the wedge in the *UVJ* color–color diagram. The Martis et al. (2016) data points for dusty and nondusty star-forming galaxies are also based on regions empirically defined on this color–color plot, calibrated using the galaxy SED dust extinctions.
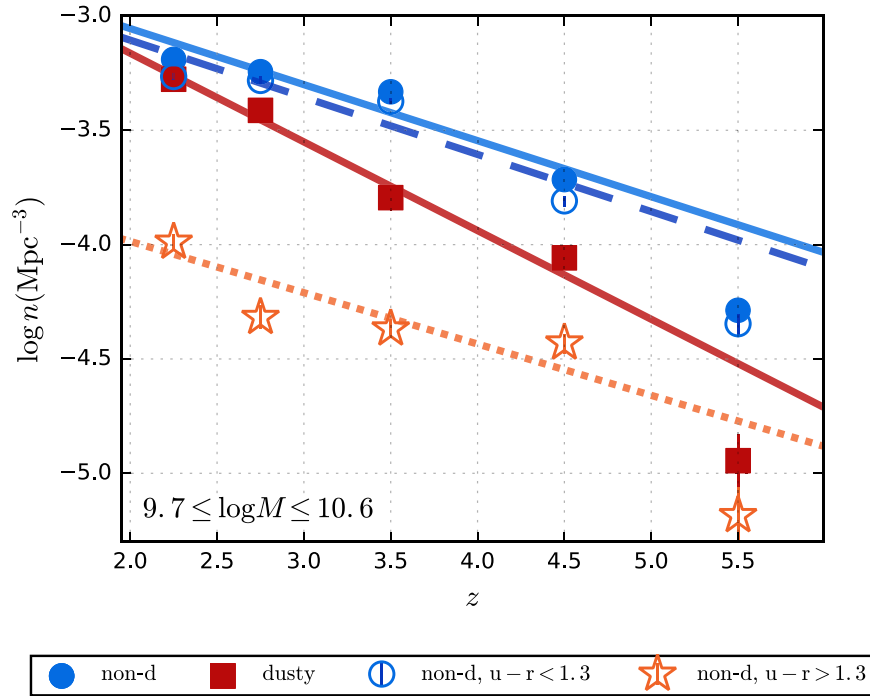

Figure 15. Number densities n of intermediate-mass galaxies (i.e., those with $9.7 < \log_{10} M_{\rm st} < 10.6\, M_\odot$) vs. redshift. Symbols are the same as in Figure 13.

Table 3
Number Densities of Intermediate Stellar Mass ($9.7 \leqslant \log_{10} M_*/M_\odot \leqslant 10.6$) Galaxies

Redshift	$n_{\rm dusty}$ (all) $10^{-4} \times {\rm Mpc}^{-3}$	$n_{\rm nondusty}$ (all) $10^{-4} \times {\rm Mpc}^{-3}$	$n_{\rm nondusty}$ (blue) $10^{-4} \times {\rm Mpc}^{-3}$	$n_{\rm nondusty}$ (red) $10^{-4} \times {\rm Mpc}^{-3}$
2.25	$5.287^{+0.198}_{-0.186}$	$6.459^{+0.234}_{-0.183}$	$5.433^{+0.208}_{-0.172}$	$1.026^{+0.084}_{-0.079}$
2.75	$3.865^{+0.169}_{-0.159}$	$5.704^{+0.205}_{-0.197}$	$5.223^{+0.190}_{-0.187}$	$0.481^{+0.061}_{-0.068}$
3.50	$1.605^{+0.083}_{-0.077}$	$4.659^{+0.120}_{-0.124}$	$4.230^{+0.119}_{-0.123}$	$0.428^{+0.043}_{-0.037}$
4.50	$0.875^{+0.059}_{-0.072}$	$1.925^{+0.087}_{-0.096}$	$1.553^{+0.078}_{-0.087}$	$0.372^{+0.037}_{-0.038}$
5.50	$0.114^{+0.034}_{-0.029}$	$0.516^{+0.047}_{-0.057}$	$0.451^{+0.044}_{-0.051}$	$0.065^{+0.021}_{-0.017}$

Facilities: Spitzer, VISTA, Subaru.
Software: SExtractor, IRAF, LePhare.

Appendix A
Photometry Comparison with Public COSMOS Catalogs

Our photometry on the ground-based images has been performed without a prior PSF matching. However, as we deal here only with $z \geqslant 2$ galaxies, we derive aperture corrections for all our magnitudes on a filter-by-filter basis, and on each stripe separately, this procedure presents no concern for our photometric measurements. To demonstrate this, in Figure 16 we compare our UltraVISTA photometry for our $z > 2$ SMUVS sources with those obtained by Muzzin et al. (2013) and Laigle et al. (2016), who have independently performed their source photometry after PSF-matching the different ground-based images.

As can be seen from the different panels in Figure 16, there is an overall good agreement between the photometric measurements performed by different groups. The photometric biases, although non-negligible, are $\leqslant 0.15$ mag in all cases. The scatter between our photometry and that of Laigle et al. (2016) is small, but it is significantly larger when compared to the photometry of Muzzin et al. (2013). Interestingly, the comparison between Laigle et al. (2016) and Muzzin et al. (2013) photometries (both obtained after PSF-matching) yields a similarly large scatter level. This results allow us to conclude that PSF-matching has a minor impact on the photometry of $z > 2$ sources and is not the main source of the (mild) discrepancies seen between different photometric measurements on ground-based images.

In Figures 17 and 18, we show a comparison of the IRAC photometry of our sources, as measured by different groups independently (Muzzin et al. 2013; Laigle et al. 2016; Straatman et al. 2016) on shallower COSMOS/IRAC maps, and our own from the SMUVS mosaics. As explained in Section 2, our IRAC photometric measurements have been obtained with a PSF-fitting technique (using the public IRAF DAOPHOT package), which assumes that all sources are point-like. The other photometric measurements have been obtained using private codes that also fit the light profiles of all sources simultaneously, but taking into account the source shapes. In Section 2 we claim that taking into account source shapes is irrelevant for the vast majority of $z > 2$ sources.

Indeed, this can be seen from Figures 17 and 18. Particularly, the middle left panel compares our SMUVS photometry with that in Laigle et al. (2016) and shows a very small bias and scatter, indicating that taking into account the source shapes does not have any major impact on the IRAC photometry. Instead, other factors (e.g., recipes to reconvert fluxes from different PSF sizes, aperture corrections) may have a much more important influence on the resulting photometry. This can be seen from the significant discrepancies among some of the photometric measurements based on different codes that do take into account the source shapes. Surprisingly, the impact of these differences on the derived statistical galaxy properties, such as the GSMF, is very small (as can be seen in Appendix B).
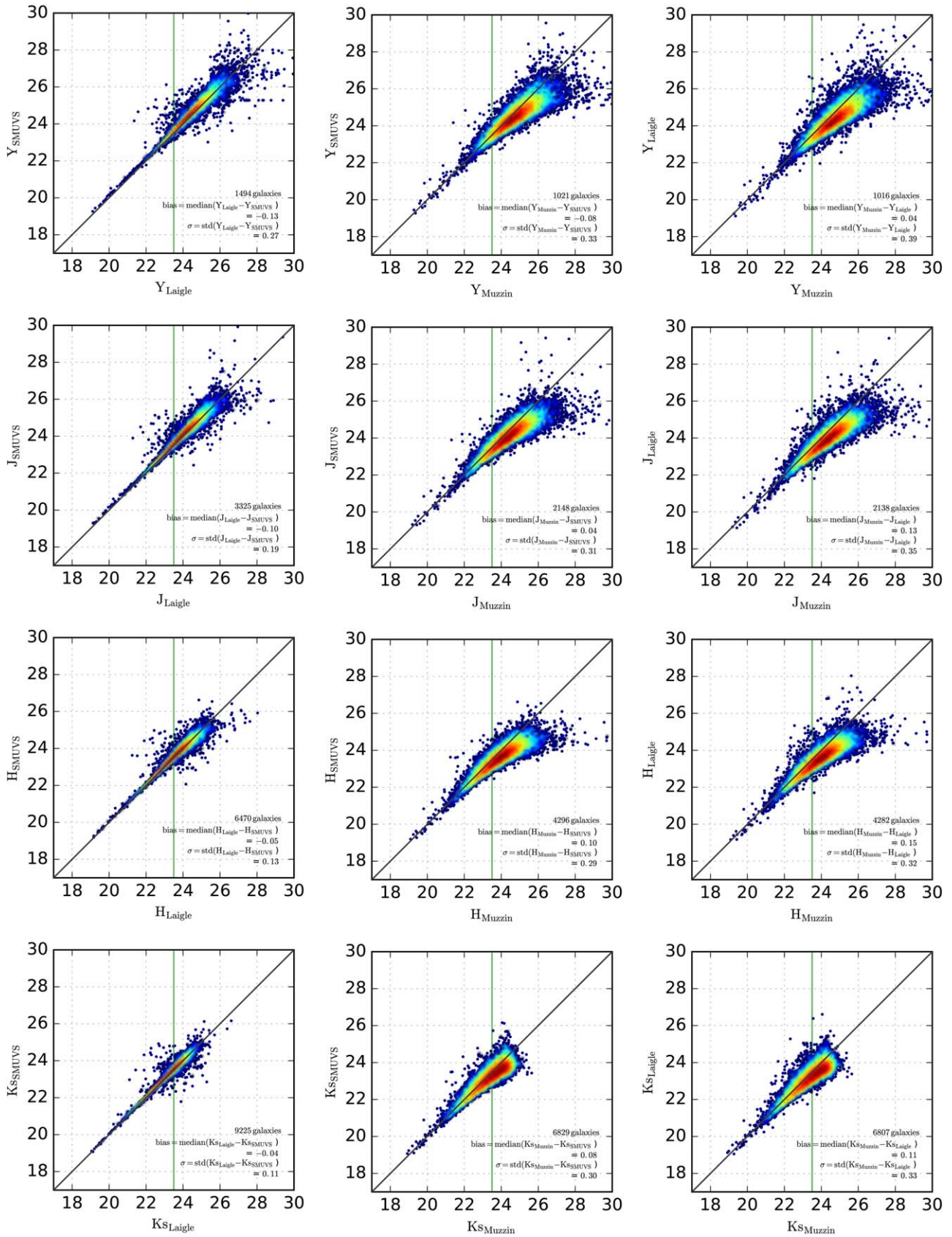
Figure 16. Comparison of our UltraVISTA photometry for our SMUVS $z \geqslant 2$ galaxies with that independently obtained by Muzzin et al. (2013) and Laigle et al. (2016) (left and middle columns), and the photometry of these two groups compared among themselves (right column). The statistics indicated in each panel label refers to sources with magnitudes <23.5, at which all three catalogs have a $\gtrsim 90\%$ completeness level.
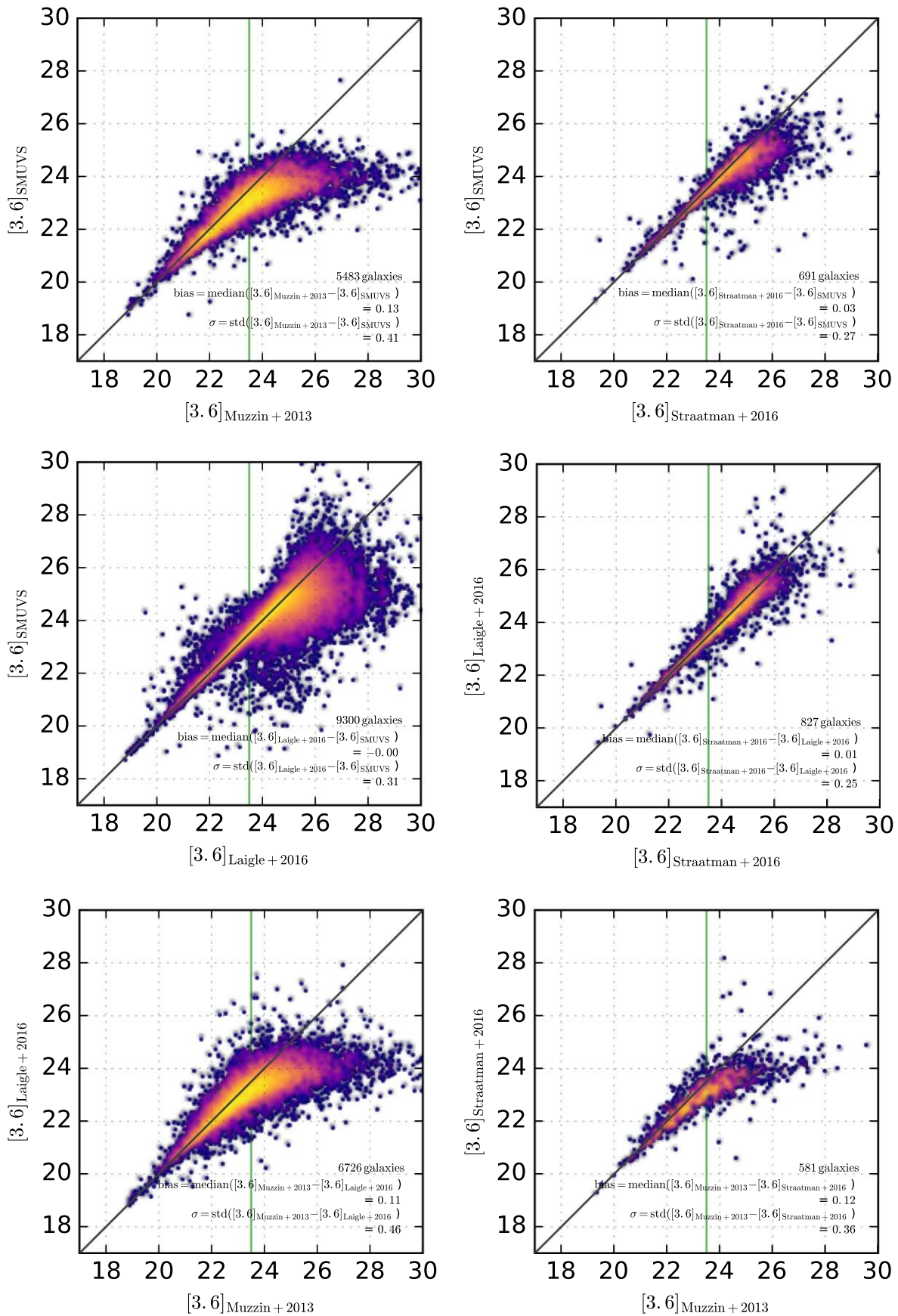
Figure 17. Comparison of total magnitudes between the IRAC 3.6 μm photometry of SMUVS $z \geqslant 2$ sources, obtained by different authors (based on shallower COSMOS/IRAC images than the SMUVS images considered here). The statistics indicated in each panel label refers to sources with magnitudes <23.5.

Figure 18. Same as Figure 17, but for IRAC 4.5 μm photometry.

Figure 19. Comparison of our total GSMF (red filled circles) with previous GSMF determinations in COSMOS and other fields. All literature GSMFs were converted to a Chabrier (2003) IMF for consistency with our own determination. Note that the data points from Grazian et al. (2015) correspond to redshift bins with $\Delta z = +0.5$ with respect to ours.
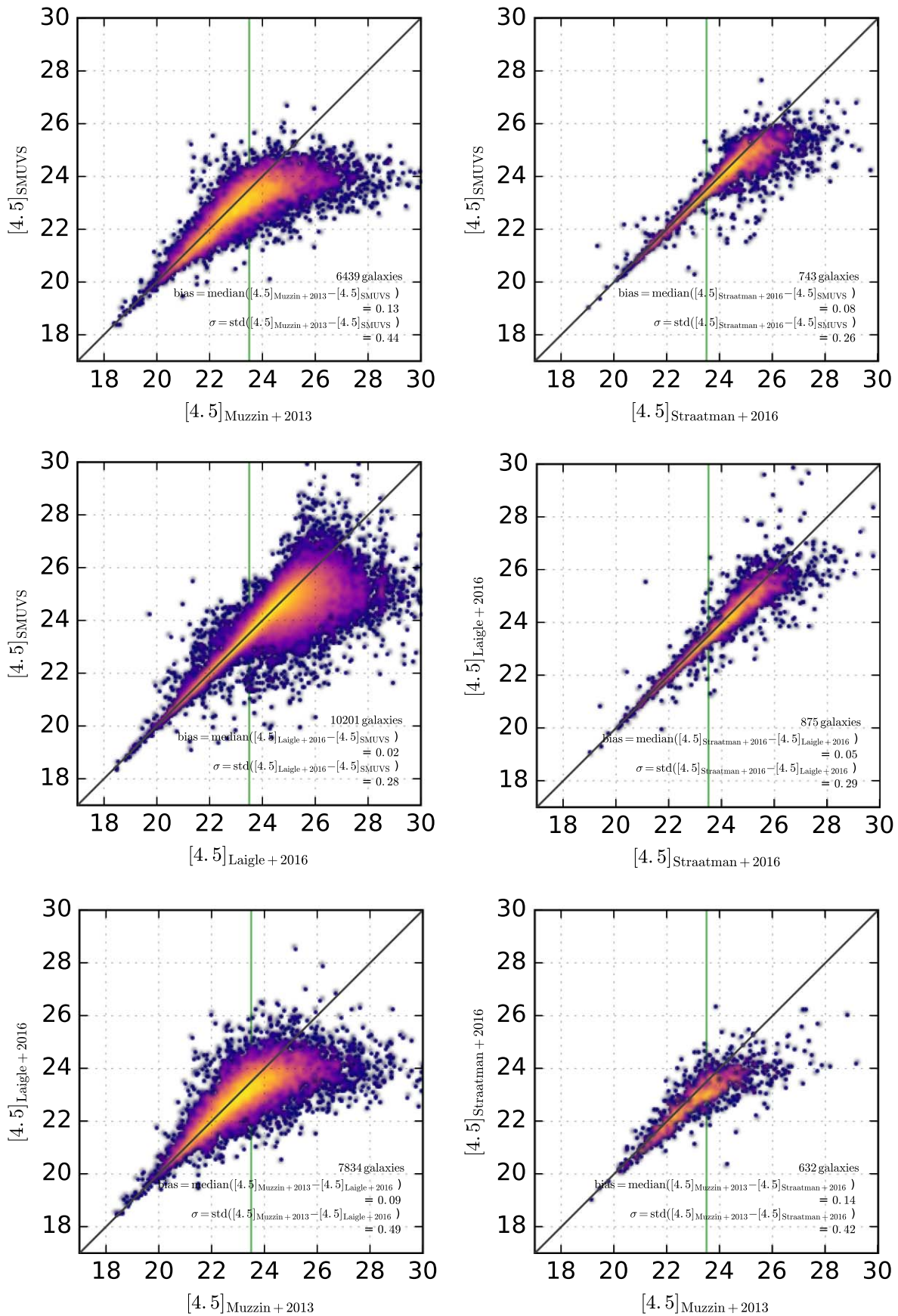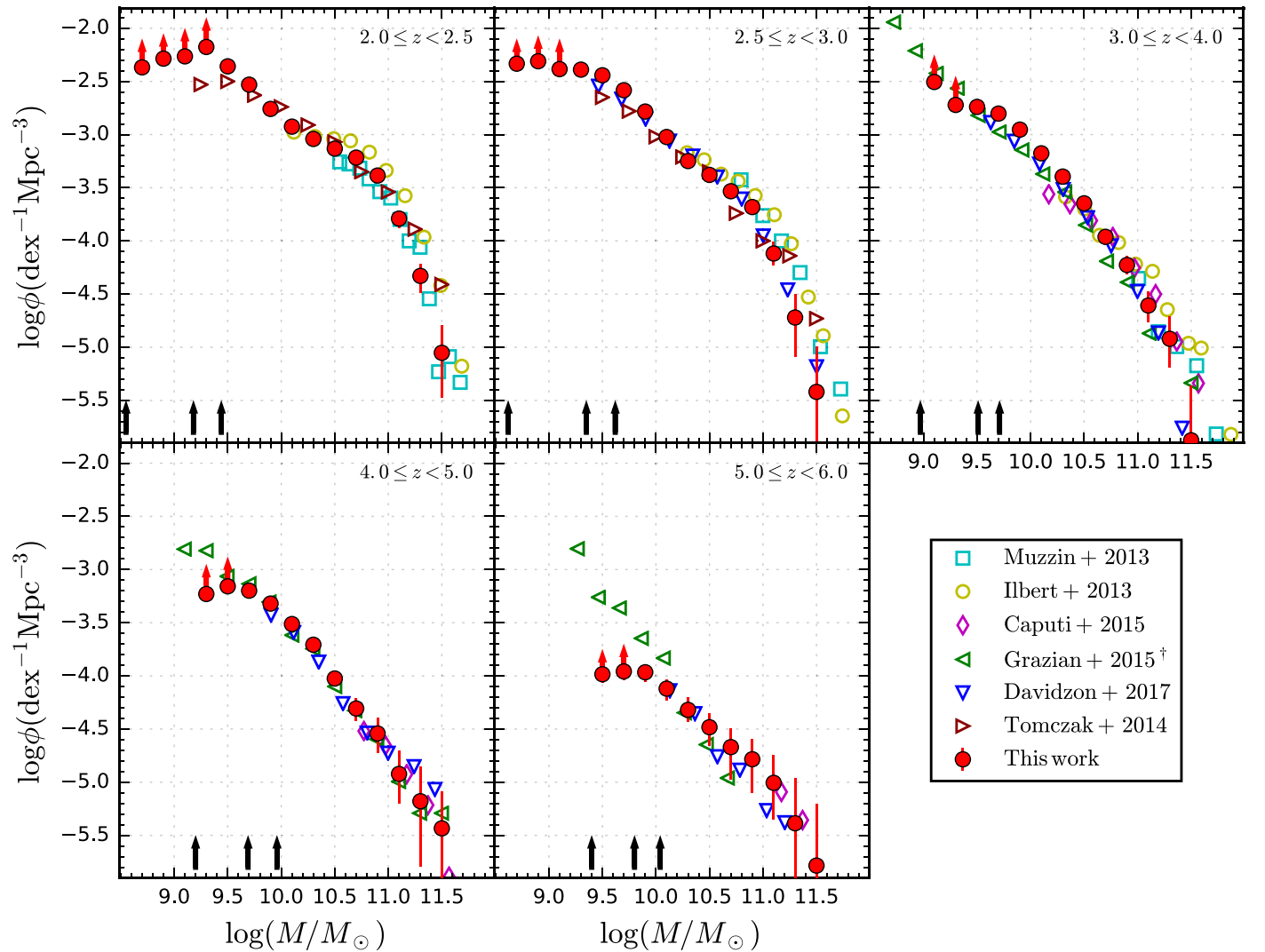
Appendix B
GSMF Comparison with Previous Works

As a sanity check, we computed the total GSMF at $z = 2$–6 and compared our results with other recent GSMF determinations in COSMOS and other fields. We show our results in Figure 19.

In the redshift range of $2.0 \leqslant z < 2.5$, our GSMF is in generally good agreement with Ilbert et al. (2013) and Muzzin et al. (2013) at $M_* \gtrsim 10^{10} M_\odot$. No comparison is possible at lower stellar masses, as these previous works are based on shallower data. Here we are able to probe galaxies down to $\sim$1.5–2.0 mag fainter, and we are able to clearly identify the intermediate-mass dip in the GSMF (e.g., Pozzetti et al. 2010) even at these high redshifts.

At $z = 3$–4 we compare our GSMF with those determined by Caputi et al. (2015) and Davidzon et al. (2017) in COSMOS and by Grazian et al. (2015) in the GOODS-South (GOODS-S) and UDS/CANDELS fields (note that the Grazian et al. [2015] data points correspond to redshift bins shifted by $\Delta z = +0.5$). We see that our GSMF is in excellent agreement with these previous determinations. The SMUVS/UltraVISTA data are only $\sim$1.5 mag shallower than the images analyzed by Grazian et al. (2015) in the UDS and the wide GOODS-S, which results in a stellar mass completeness limit only $\sim$0.5 dex larger, as can be seen in Figure 19.

At $z = 4$–6, our GSMF is in very good agreement with previous works at high and intermediate stellar masses down to $\log_{10}(M_*/M_\odot) \lesssim 9.2$–9.5. Below these stellar masses, our sample suffers from significant incompleteness.

Appendix C
Errors on the GSMF

In Figure 20, we show the contribution of each source of uncertainty to the total GSMF. The uncertainties are dominated by Poissonian errors at the high-mass end. At higher redshifts, the contributions from σ_{MC} and σ_{cv} become increasingly more important.
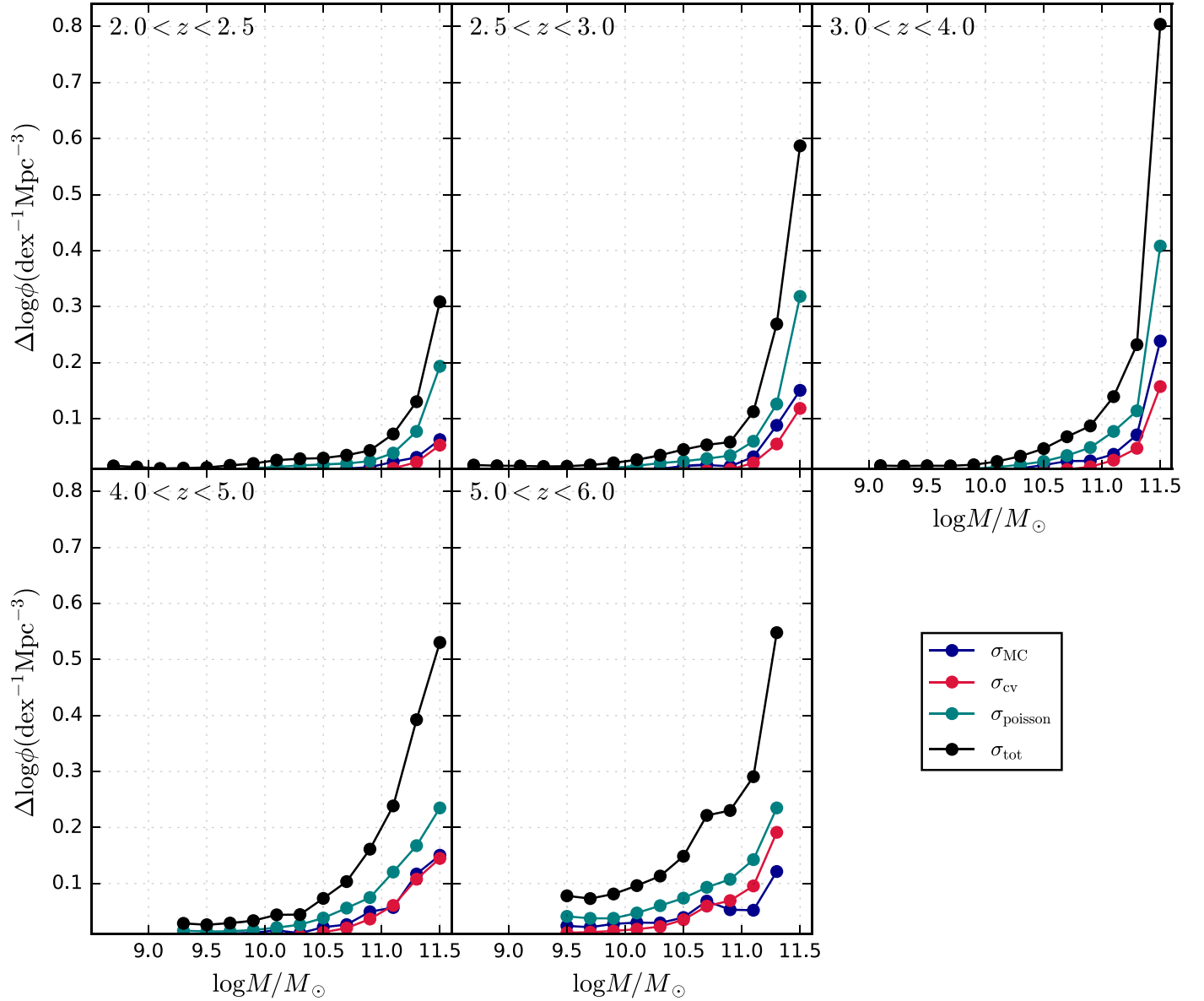

Figure 20. Contribution of each source of uncertainty to the total GSMF (Poisson ($\sigma_{poisson}$), cosmic variance (σ_{CV}) and uncertainties arising from Monte Carlo (σ_{MC}) realizations of photometry.)

Appendix D
GSMF

In Tables 4–6 we present the GSMF values at $2.0 \leqslant z < 3.0$, $3.0 \leqslant z < 5.0$, and $5.0 \leqslant z \leqslant 6.0$. We quote the dusty, nondusty, nondusty blue, and nondusty red GSMF components separately.

Table 4
Tabulated Values of GSMFs for $2.0 \leqslant z < 3.0$

$\log M/M_{\odot}$	$2.0 \leqslant z < 2.5$				$2.5 \leqslant z < 3.0$			
	Φ_{d} [a]	Φ_{nd} [b]	Φ_{nd-b} [c]	Φ_{nd-r} [d]	Φ_{d}	Φ_{nd}	Φ_{nd-b}	Φ_{nd-r}
8.7	$4.257^{+0.386}_{-0.359}$	$38.584^{+1.516}_{-1.642}$	$36.744^{+1.735}_{-1.672}$	$1.839^{+0.368}_{-0.353}$	$9.332^{+0.559}_{-0.587}$	$37.065^{+2.229}_{-1.849}$	$36.698^{+2.180}_{-1.673}$	$0.367^{+0.192}_{-0.181}$
8.9	$3.646^{+0.369}_{-0.395}$	$48.109^{+1.641}_{-1.490}$	$46.382^{+1.615}_{-1.515}$	$1.726^{+0.315}_{-0.374}$	$11.756^{+0.721}_{-0.561}$	$37.161^{+1.754}_{-1.708}$	$35.923^{+1.740}_{-1.673}$	$1.239^{+0.322}_{-0.279}$
9.1	$3.507^{+0.414}_{-0.383}$	$50.871^{+1.408}_{-1.310}$	$49.483^{+1.257}_{-1.412}$	$1.388^{+0.223}_{-0.251}$	$10.420^{+0.697}_{-0.577}$	$30.824^{+1.407}_{-1.135}$	$29.725^{+1.325}_{-1.278}$	$1.100^{+0.310}_{-0.268}$
9.3	$3.507^{+0.398}_{-0.320}$	$63.118^{+1.600}_{-1.947}$	$61.608^{+1.641}_{-1.948}$	$1.510^{+0.231}_{-0.249}$	$7.993^{+0.521}_{-0.556}$	$32.784^{+1.366}_{-1.157}$	$31.498^{+1.369}_{-1.118}$	$1.287^{+0.254}_{-0.223}$
9.5	$4.432^{+0.383}_{-0.423}$	$39.364^{+1.187}_{-1.214}$	$38.500^{+1.113}_{-1.330}$	$0.865^{+0.207}_{-0.190}$	$5.369^{+0.475}_{-0.457}$	$30.725^{+1.146}_{-1.053}$	$29.507^{+1.075}_{-1.054}$	$1.218^{+0.217}_{-0.217}$
9.7	$5.972^{+0.453}_{-0.555}$	$23.482^{+1.003}_{-0.917}$	$22.747^{+0.927}_{-0.979}$	$0.735^{+0.175}_{-0.162}$	$5.020^{+0.533}_{-0.479}$	$21.107^{+1.014}_{-0.901}$	$20.108^{+0.878}_{-0.920}$	$1.000^{+0.205}_{-0.178}$
9.9	$6.348^{+0.443}_{-0.538}$	$11.074^{+0.647}_{-0.605}$	$10.175^{+0.610}_{-0.606}$	$0.900^{+0.200}_{-0.160}$	$5.381^{+0.496}_{-0.515}$	$11.071^{+0.663}_{-0.616}$	$10.538^{+0.668}_{-0.591}$	$0.533^{+0.154}_{-0.133}$
10.1	$6.525^{+0.458}_{-0.463}$	$5.347^{+0.457}_{-0.393}$	$4.257^{+0.384}_{-0.368}$	$1.090^{+0.212}_{-0.184}$	$4.839^{+0.499}_{-0.406}$	$4.646^{+0.483}_{-0.434}$	$4.303^{+0.409}_{-0.390}$	$0.343^{+0.145}_{-0.092}$
10.3	$5.765^{+0.491}_{-0.503}$	$3.332^{+0.366}_{-0.340}$	$2.002^{+0.262}_{-0.273}$	$1.330^{+0.229}_{-0.202}$	$3.605^{+0.385}_{-0.343}$	$2.031^{+0.280}_{-0.266}$	$1.485^{+0.225}_{-0.270}$	$0.546^{+0.180}_{-0.150}$
10.5	$4.476^{+0.462}_{-0.436}$	$2.902^{+0.301}_{-0.329}$	$1.457^{+0.252}_{-0.221}$	$1.444^{+0.207}_{-0.250}$	$2.716^{+0.308}_{-0.352}$	$1.460^{+0.230}_{-0.257}$	$0.863^{+0.187}_{-0.184}$	$0.597^{+0.158}_{-0.171}$
10.7	$3.573^{+0.354}_{-0.359}$	$2.496^{+0.324}_{-0.294}$	$0.874^{+0.219}_{-0.190}$	$1.622^{+0.247}_{-0.233}$	$1.752^{+0.310}_{-0.260}$	$1.180^{+0.260}_{-0.215}$	$0.533^{+0.154}_{-0.139}$	$0.647^{+0.165}_{-0.184}$
10.9	$2.243^{+0.321}_{-0.290}$	$1.875^{+0.265}_{-0.280}$	$0.519^{+0.167}_{-0.137}$	$1.356^{+0.239}_{-0.227}$	$1.130^{+0.234}_{-0.233}$	$0.952^{+0.217}_{-0.206}$	$0.241^{+0.130}_{-0.111}$	$0.711^{+0.180}_{-0.158}$
11.1	$0.760^{+0.214}_{-0.183}$	$0.862^{+0.229}_{-0.171}$	$0.228^{+0.117}_{-0.088}$	$0.634^{+0.167}_{-0.166}$	$0.508^{+0.203}_{-0.140}$	$0.254^{+0.133}_{-0.116}$	$0.038^{+0.069}_{-0.038}$	$0.216^{+0.112}_{-0.079}$
11.3	$0.203^{+0.109}_{-0.091}$	$0.266^{+0.117}_{-0.115}$	$0.025^{+0.056}_{-0.025}$	$0.241^{+0.113}_{-0.097}$	$0.152^{+0.121}_{-0.086}$	$0.038^{+0.062}_{-0.038}$	$0.013^{+0.037}_{-0.013}$	$0.025^{+0.058}_{-0.025}$
11.5	$0.051^{+0.079}_{-0.045}$	$0.038^{+0.060}_{-0.038}$	$0.025^{+0.040}_{-0.035}$	$0.013^{+0.050}_{-0.013}$	$0.025^{+0.058}_{-0.025}$	$0.013^{+0.037}_{-0.013}$	...	$0.013^{+0.053}_{-0.013}$

Notes. All number densities are in units of $10^{-4} \times \mathrm{Mpc}^{-3} \, \mathrm{dex}^{-1}$. Uncertainties include Poisson noise, SED modeling uncertainties, and cosmic variance.
[a] Dusty.
[b] Nondusty all.
[c] Nondusty blue.
[d] Nondusty red.

Table 5
Tabulated Values of GSMFs for $3.0 \leqslant z < 5.0$

$\log M/M_{\odot}$	$3.0 \leqslant z < 4.0$				$4.0 \leqslant z < 5.0$			
	Φ_{d}	Φ_{nd}	Φ_{nd-b}	Φ_{nd-r}	Φ_{d}	Φ_{nd}	Φ_{nd-b}	Φ_{nd-r}
9.1	$4.867^{+0.295}_{-0.325}$	$26.366^{+1.368}_{-1.264}$	$25.553^{+1.143}_{-1.085}$	$0.813^{+0.213}_{-0.173}$	...	...	...	...
9.3	$3.990^{+0.271}_{-0.310}$	$15.005^{+0.567}_{-0.587}$	$13.840^{+0.519}_{-0.587}$	$1.165^{+0.185}_{-0.161}$	$2.665^{+0.263}_{-0.256}$	$3.223^{+0.318}_{-0.308}$	$3.104^{+0.277}_{-0.318}$	$0.119^{+0.108}_{-0.104}$
9.5	$2.786^{+0.260}_{-0.285}$	$15.416^{+0.546}_{-0.567}$	$14.027^{+0.541}_{-0.500}$	$1.389^{+0.180}_{-0.194}$	$2.689^{+0.236}_{-0.226}$	$4.266^{+0.317}_{-0.336}$	$3.807^{+0.307}_{-0.322}$	$0.458^{+0.125}_{-0.96}$
9.7	$2.137^{+0.228}_{-0.220}$	$13.609^{+0.583}_{-0.503}$	$12.329^{+0.566}_{-0.486}$	$1.280^{+0.153}_{-0.177}$	$1.878^{+0.211}_{-0.259}$	$4.451^{+0.351}_{-0.317}$	$3.902^{+0.339}_{-0.261}$	$0.549^{+0.145}_{-0.119}$
9.9	$2.137^{+0.223}_{-0.240}$	$8.991^{+0.405}_{-0.405}$	$8.265^{+0.375}_{-0.406}$	$0.726^{+0.114}_{-0.123}$	$1.435^{+0.228}_{-0.933}$	$3.350^{+0.302}_{-0.305}$	$2.690^{+0.242}_{-0.279}$	$0.659^{+0.131}_{-0.128}$
10.1	$1.897^{+0.191}_{-0.253}$	$4.764^{+0.318}_{-0.333}$	$4.389^{+0.289}_{-0.321}$	$0.375^{+0.091}_{-0.083}$	$0.965^{+0.165}_{-0.181}$	$2.106^{+0.260}_{-0.236}$	$1.693^{+0.230}_{-0.239}$	$0.413^{+0.104}_{-0.093}$
10.3	$1.735^{+0.205}_{-0.193}$	$2.290^{+0.217}_{-0.215}$	$2.057^{+0.203}_{-0.207}$	$0.234^{+0.074}_{-0.066}$	$0.692^{+0.141}_{-0.133}$	$1.271^{+0.169}_{-0.171}$	$1.018^{+0.173}_{-0.145}$	$0.252^{+0.086}_{-0.068}$
10.5	$1.139^{+0.186}_{-0.160}$	$1.118^{+0.152}_{-0.146}$	$0.924^{+0.129}_{-0.136}$	$0.194^{+0.072}_{-0.063}$	$0.354^{+0.116}_{-0.115}$	$0.591^{+0.167}_{-0.125}$	$0.385^{+0.137}_{-0.091}$	$0.206^{+0.076}_{-0.074}$
10.7	$0.694^{+0.133}_{-0.133}$	$0.398^{+0.108}_{-0.100}$	$0.238^{+0.079}_{-0.070}$	$0.160^{+0.071}_{-0.062}$	$0.339^{+0.104}_{-0.105}$	$0.155^{+0.081}_{-0.069}$	$0.118^{+0.078}_{-0.062}$	$0.037^{+0.049}_{-0.037}$
10.9	$0.247^{+0.085}_{-0.092}$	$0.347^{+0.090}_{-0.089}$	$0.207^{+0.077}_{-0.068}$	$0.140^{+0.069}_{-0.052}$	$0.214^{+0.095}_{-0.084}$	$0.074^{+0.060}_{-0.049}$	$0.044^{+0.053}_{-0.032}$	$0.029^{+0.040}_{-0.029}$
11.1	$0.140^{+0.079}_{-0.055}$	$0.107^{+0.058}_{-0.057}$	$0.053^{+0.058}_{-0.035}$	$0.053^{+0.049}_{-0.039}$	$0.098^{+0.069}_{-0.055}$	$0.022^{+0.039}_{-0.022}$	$0.015^{+0.036}_{-0.015}$	$0.007^{+0.023}_{-0.007}$
11.3	$0.100^{+0.058}_{-0.057}$	$0.020^{+0.033}_{-0.020}$	$0.020^{+0.033}_{-0.020}$	...	$0.066^{+0.062}_{-0.052}$	...	...	...
11.5	$0.007^{+0.028}_{-0.007}$	$0.007^{+0.028}_{-0.007}$	...	$0.007^{+0.028}_{-0.007}$	$0.037^{+0.045}_{-0.037}$	...	...	...

Table 6
Tabulated Values of GSMFs for $5.0 \leqslant z < 6.0$

$\log M/M_\odot$	$5.0 \leqslant z \leqslant 6.0$			
	Φ_d	Φ_{nd}	Φ_{nd-b}	Φ_{nd-r}
9.5	$0.197^{+0.097}_{-0.079}$	$0.839^{+0.207}_{-0.182}$	$0.810^{+0.206}_{-0.165}$	$0.029^{+0.043}_{-0.032}$
9.7	$0.230^{+0.094}_{-0.084}$	$0.871^{+0.179}_{-0.167}$	$0.808^{+0.176}_{-0.173}$	$0.064^{+0.052}_{-0.048}$
9.9	$0.206^{+0.104}_{-0.071}$	$0.876^{+0.189}_{-0.163}$	$0.773^{+0.183}_{-0.140}$	$0.103^{+0.070}_{-0.056}$
10.1	$0.115^{+0.082}_{-0.071}$	$0.644^{+0.161}_{-0.171}$	$0.586^{+0.141}_{-0.151}$	$0.058^{+0.049}_{-0.047}$
10.3	$0.107^{+0.069}_{-0.059}$	$0.372^{+0.129}_{-0.100}$	$0.282^{+0.126}_{-0.091}$	$0.091^{+0.058}_{-0.054}$
10.5	$0.058^{+0.062}_{-0.058}$	$0.272^{+0.111}_{-0.110}$	$0.222^{+0.100}_{-0.056}$	$0.049^{+0.060}_{-0.047}$
10.7	$0.066^{+0.067}_{-0.054}$	$0.148^{+0.084}_{-0.079}$	$0.115^{+0.077}_{-0.064}$	$0.033^{+0.047}_{-0.033}$
10.9	$0.115^{+0.080}_{-0.067}$	$0.049^{+0.066}_{-0.040}$	$0.049^{+0.054}_{-0.040}$	$\cdots$
11.1	$0.074^{+0.063}_{-0.061}$	$0.025^{+0.036}_{-0.025}$	$0.025^{+0.036}_{-0.032}$	$\cdots$
11.3	$0.033^{+0.066}_{-0.033}$	$0.008^{+0.042}_{-0.008}$	$0.008^{+0.042}_{-0.008}$	$\cdots$
11.5	$\cdots$	$0.016^{+0.046}_{-0.016}$	$0.008^{+0.042}_{-0.008}$	$0.008^{+0.029}_{-0.008}$

ORCID iDs

S. Deshmukh ⓘ https://orcid.org/0000-0001-7264-6925
K. I. Caputi ⓘ https://orcid.org/0000-0001-8183-1460
M. L. N. Ashby ⓘ https://orcid.org/0000-0002-3993-0745
H. J. McCracken ⓘ https://orcid.org/0000-0002-9489-7765
J. P. U. Fynbo ⓘ https://orcid.org/0000-0002-8149-8298
B. Milvang-Jensen ⓘ https://orcid.org/0000-0002-2281-2785
O. Ilbert ⓘ https://orcid.org/0000-0002-7303-4397

References

Adelberger, K. L., & Steidel, C. C. 2000, ApJ, 544, 218
Arnouts, S., Cristiani, S., Moscardini, L., et al. 1999, MNRAS, 310, 540
Ashby, M. L. N., Willner, S. P., Fazio, G. G., et al. 2013, ApJ, 769, 80
Ashby, M. L. N., Willner, S. P., Fazio, G. G., et al. 2015, ApJS, 218, 33
Baldry, I. K., Glazebrook, K., Brinkmann, J., et al. 2004, ApJ, 600, 681
Bertin, E., & Arnouts, S. 1996, A&AS, 117, 393
Bielby, R., Hudelot, P., McCracken, H. J., et al. 2012, A&A, 545, A23
Brinchmann, J., & Ellis, R. S. 2000, ApJL, 536, L77
Bruzual, G., & Charlot, S. 2003, MNRAS, 344, 1000
Calura, F., Pozzi, F., Cresci, G., et al. 2017, MNRAS, 465, 54
Calzetti, D., Armus, L., Bohlin, R. C., et al. 2000, ApJ, 533, 682
Caputi, K. I., Cirasuolo, M., Dunlop, J. S., et al. 2011, MNRAS, 413, 162
Caputi, K. I., Deshmukh, S., Ashby, M. L. N., et al. 2017, ApJ, 849, 45
Caputi, K. I., Ilbert, O., Laigle, C., et al. 2015, ApJ, 810, 73
Caputi, K. I., Lagache, G., Yan, L., et al. 2007, ApJ, 660, 97
Casey, C. M., Narayanan, D., & Cooray, A. 2014, PhR, 541, 45
Cassata, P., Giavalisco, M., Williams, C. C., et al. 2013, ApJ, 775, 106
Cattaneo, A., Dekel, A., Faber, S. M., & Guiderdoni, B. 2008, MNRAS, 389, 567
Chabrier, G. 2003, PASP, 115, 763
Civano, F., Marchesi, S., Comastri, A., et al. 2016, ApJ, 819, 62
Comparat, J., Richard, J., Kneib, J.-P., et al. 2015, A&A, 575, A40
Cowley, W. I., Caputi, K. I., & Deshmukh, S. 2018, ApJ
Cucciati, O., Tresse, L., Ilbert, O., et al. 2012, A&A, 539, A31
Cullen, F., McLure, R. J., Khochfar, S., et al. 2018, MNRAS, 476, 3218
Davidzon, I., Ilbert, O., Laigle, C., et al. 2017, A&A, 605, A70
Duncan, K., Conselice, C. J., Mortlock, A., et al. 2014, MNRAS, 444, 2960
Eddington, A. S. 1913, MNRAS, 73, 359
Fazio, G. G., Hora, J. L., Allen, L. E., et al. 2004, ApJS, 154, 10
Feldmann, R., Quataert, E., Hopkins, P. F., Faucher-Giguère, C.-A., & Kereš, D. 2017, MNRAS, 470, 1050
Fumagalli, M., Labbé, I., Patel, S. G., et al. 2014, ApJ, 796, 35
Gabor, J. M., Davé, R., Oppenheimer, B. D., & Finlator, K. 2011, MNRAS, 417, 2676
Gavilan, L., Lemaire, J. L., & Vidali, G. 2012, MNRAS, 424, 2961
Gehrels, N. 1986, ApJ, 303, 336
Gould, R. J., & Salpeter, E. E. 1963, ApJ, 138, 393
Grazian, A., Fontana, A., Santini, P., et al. 2015, A&A, 575, A96
Gruppioni, C., Pozzi, F., Andreani, P., et al. 2010, A&A, 518, L27
Heinis, S., Buat, V., Béthermin, M., et al. 2013, MNRAS, 429, 1113
Helgason, K., Ricotti, M., & Kashlinsky, A. 2012, ApJ, 752, 113
Hill, A. R., Muzzin, A., Franx, M., et al. 2017, ApJ, 837, 147
Hollenbach, D., & Salpeter, E. E. 1971, ApJ, 163, 155
Hopkins, P. F., Torrey, P., Faucher-Giguère, C.-A., Quataert, E., & Murray, N. 2016, MNRAS, 458, 816
Hughes, D. H., Serjeant, S., Dunlop, J., et al. 1998, Natur, 394, 241
Ilbert, O., Arnouts, S., McCracken, H. J., et al. 2006, A&A, 457, 841
Ilbert, O., McCracken, H. J., Le Fèvre, O., et al. 2013, A&A, 556, A55
Juneau, S., Glazebrook, K., Crampton, D., et al. 2005, ApJL, 619, L135
Kajisawa, M., Ichikawa, T., Yoshikawa, T., et al. 2011, PASJ, 63, 403
Kodama, T., Yamada, T., Akiyama, M., et al. 2004, MNRAS, 350, 1005
Laigle, C., McCracken, H. J., Ilbert, O., et al. 2016, ApJS, 224, 24
Le Fèvre, O., Tasca, L. A. M., Cassata, P., et al. 2015, A&A, 576, A79
Lilly, S. J., Le Fèvre, O., Renzini, A., et al. 2007, ApJS, 172, 70
Magnelli, B., Elbaz, D., Chary, R. R., et al. 2011, A&A, 528, A35
Mancini, C., Matute, I., Cimatti, A., et al. 2009, A&A, 500, 705
Martis, N. S., Marchesini, D., Brammer, G. B., et al. 2016, ApJL, 827, L25
McCracken, H. J., Milvang-Jensen, B., Dunlop, J., et al. 2012, A&A, 544, A156
Merlin, E., Fontana, A., Castellano, M., et al. 2018, MNRAS, 473, 2098
Merlin, E., Fontana, A., Ferguson, H. C., et al. 2015, A&A, 582, A15
Moster, B. P., Somerville, R. S., Newman, J. A., & Rix, H.-W. 2011, ApJ, 731, 113
Muzzin, A., Marchesini, D., Stefanon, M., et al. 2013, ApJ, 777, 18
Oke, J. B., & Gunn, J. E. 1983, ApJ, 266, 713
Pannella, M., Carilli, C. L., Daddi, E., et al. 2009, ApJL, 698, L116
Popping, G., Somerville, R. S., & Galametz, M. 2017, MNRAS, 471, 3152
Pozzetti, L., Bolzonella, M., Zucca, E., et al. 2010, A&A, 523, A13
Reddy, N. A., Pettini, M., Steidel, C. C., et al. 2012, ApJ, 754, 25
Sanders, D. B., Salvato, M., Aussel, H., et al. 2007, ApJS, 172, 86
Santini, P., Fontana, A., Grazian, A., et al. 2012, A&A, 538, A33
Schechter, P. 1976, ApJ, 203, 297
Schmidt, M. 1968, ApJ, 151, 393
Scoville, N., Aussel, H., Brusa, M., et al. 2007, ApJS, 172, 1
Somerville, R. S., & Davé, R. 2015, ARA&A, 53, 51
Sommariva, V., Fontana, A., Lamastra, A., et al. 2014, A&A, 571, A99
Song, M., Finkelstein, S. L., Ashby, M. L. N., et al. 2016, ApJ, 825, 5
Steinhardt, C. L., Speagle, J. S., Capak, P., et al. 2014, ApJL, 791, L25
Straatman, C. M. S., Labbé, I., Spitler, L. R., et al. 2014, ApJL, 783, L14
Straatman, C. M. S., Labbé, I., Spitler, L. R., et al. 2015, ApJL, 808, L29
Straatman, C. M. S., Spitler, L. R., Quadri, R. F., et al. 2016, ApJ, 830, 51
Taniguchi, Y., Scoville, N., Murayama, T., et al. 2007, ApJS, 172, 9
Tomczak, A. R., Quadri, R. F., Tran, K.-V. H., et al. 2014, ApJ, 783, 85
Werner, M. W., Roellig, T. L., Low, F. J., et al. 2004, ApJS, 154, 1